

ForestFlow: cosmological emulation of Lyman- α forest clustering from linear to nonlinear scales

J. Chaves-Montero¹[★], L. Cabayol-Garcia^{1,2}[†], M. Lokken¹, A. Font-Ribera¹, and others

¹*Institut de Física d'Altes Energies (IFAE), The Barcelona Institute of Science and Technology, 08193 Bellaterra (Barcelona), Spain*

²*Port d'Informació Científica, Campus UAB, C. Albareda s/n, 08193 Bellaterra (Barcelona), Spain*

Accepted XXX. Received YYY; in original form ZZZ

ABSTRACT

On large scales, measurements of the Lyman- α forest offer insights into the expansion history of the Universe, while on small scales, these impose strict constraints on the growth history, the nature of dark matter, and the sum of neutrino masses. This work introduces FORESTFLOW, a cosmological emulator designed to bridge the gap between large- and small-scale analyses. Using conditional normalizing flows, FORESTFLOW emulates the 2 Lyman- α linear biases and 6 parameters describing small-scale deviations of the three-dimensional flux power spectrum (P_{3D}) from linear theory. These 8 parameters are modeled as a function of cosmology — the small-scale amplitude and slope of the linear power spectrum — and the physics of the intergalactic medium. Thus, in combination with a Boltzmann solver, FORESTFLOW can predict P_{3D} on arbitrarily large (linear) scales and the one-dimensional flux power spectrum (P_{1D}) — the primary observable for small-scale analyses — without the need for interpolation or extrapolation. Trained on a suite of 30 fixed-and-paired cosmological hydrodynamical simulations spanning redshifts from $z = 2$ to 4.5, FORESTFLOW achieves 3 and 1.5% precision in describing P_{3D} and P_{1D} from linear scales to $k = 5 \text{ Mpc}^{-1}$ and $k_{\parallel} = 4 \text{ Mpc}^{-1}$, respectively. Thanks to its parameterization, the precision of the emulator is similar for two extensions to the Λ CDM model — massive neutrinos and curvature — and ionization histories not included in the training set. FORESTFLOW will be crucial for the cosmological analysis of Lyman- α forest measurements from the DESI survey and facilitate novel multiscale analyses.

Key words: quasars: absorption lines – cosmology: large-scale structure of Universe – methods: statistical

1 INTRODUCTION

The Lyman- α forest refers to absorption lines in the spectra of high-redshift quasars resulting from Lyman- α absorption by neutral hydrogen in the intergalactic medium (IGM; for a review, see McQuinn 2016). Even though quasars can be observed at very high redshifts with relatively short exposure times, the scarcity of these sources limits their direct use for precision cosmology. Conversely, Lyman- α forest measurements from a single quasar spectrum provide information about density fluctuations over hundreds of megaparsecs along the line of sight, making this observable an excellent tracer of large-scale structure at high redshifts.

Cosmological analyses of the Lyman- α forest rely on either three-dimensional correlations of the Lyman- α transmission field (ξ_{3D} ; e.g.; Slosar et al. 2011) or correlations along the line-of-sight of each quasar; i.e., the one-dimensional flux power spectrum (P_{1D} ; e.g.; Croft et al. 1998; McDonald et al. 2000b). The first analyses set constraints on the expansion history of the Universe by measuring baryonic acoustic oscillations (BAO; e.g.; Busca et al. 2013; Slosar et al. 2013; du Mas des Bourboux et al. 2020), for which linear

or perturbation theory is accurate enough. On the other hand, P_{1D} analyses measure the small-scale amplitude and slope of the linear power spectrum (e.g.; Croft et al. 1998; McDonald et al. 2000b; Zaldarriaga et al. 2001; Viel et al. 2004; McDonald et al. 2005), the nature of dark matter (e.g.; Seljak et al. 2006a; Viel et al. 2013; Iršič et al. 2017; Palanque-Delabrouille et al. 2020; Rogers & Peiris 2021b), the thermal history of the IGM (e.g.; Viel & Haehnelt 2006; Bolton et al. 2008; Lee et al. 2015; Walther et al. 2019) and the reionization history of the Universe (see the reviews Meiksin 2009; McQuinn 2016). In combination with cosmic microwave background constraints, P_{1D} analyses also set tight constraints on the sum of neutrino masses and the running of the spectral index (e.g.; Spergel et al. 2003; Verde et al. 2003; Viel et al. 2004; Seljak et al. 2005, 2006b; Palanque-Delabrouille et al. 2015, 2020).

Unlike ξ_{3D} studies, P_{1D} analyses go deep into the nonlinear regime and require time-demanding hydrodynamical simulations (e.g.; Cen et al. 1994; Miralda-Escudé et al. 1996; Meiksin et al. 2001; Lukić et al. 2015; Walther et al. 2021; Chabanier et al. 2023). Naive analyses would demand running millions of hydrodynamical simulations, which is currently unfeasible. Rather, the preferred solution is constructing fast surrogate models that make precise predictions across the input parameter space using simulation measurements as the training set. The main advantage of these surrogate models,

★ jchaves@ifae.es

† lcabayol@pic.es

known as emulators, is reducing the number of simulations required for Bayesian inference from millions to dozens or hundreds. In the context of Lyman- α forest studies, the first P_{1D} emulators involved simple linear interpolation (McDonald et al. 2006) and progressively moved towards using Gaussian processes (GPs; Sacks et al. 1989; MacKay et al. 1998) and neural networks (NNs; McCulloch & Pitts 1943); for instance, Bird et al. (2019); Rogers et al. (2019); Walther et al. (2019); Pedersen et al. (2021); Takhtaganov et al. (2021); Rogers & Peiris (2021a); Fernandez et al. (2022); Bird et al. (2023); Molaro et al. (2023); Cabayol-Garcia et al. (2023).

The primary purpose of this work is to provide consistent predictions for Lyman- α forest clustering from linear to nonlinear scales. There are three main approaches to achieve this. The first relies on perturbation theory (e.g.; Givans & Hirata 2020; Chen et al. 2021; Ivanov 2024), which delivers precise predictions on perturbative scales at the cost of marginalizing over a large number of free parameters. The second involves emulating power spectrum modes measured from a suite of cosmological hydrodynamical simulations, which provides precise predictions from quasilinear to nonlinear scales. The main limitation of this approach is that accessing the largest scales used in BAO analyses, $r \simeq 300$ Mpc, would require hydrodynamical simulations at least 3 times larger than this scale (e.g.; Angulo et al. 2008), which is currently unfeasible due to the computational demands of these simulations.

Instead, we follow the third approach of emulating the best-fitting parameters of a physically-motivated Lyman- α clustering model to measurements from a suite of cosmological hydrodynamical simulations (see McDonald 2003; Arinyo-i-Prats et al. 2015). We emulate the 2 Lyman- α linear biases, which completely set the large-scale behavior of P_{3D} together with the linear power spectrum, and 6 parameters modeling small-scale deviations of P_{3D} from linear theory. Consequently, this strategy has the potential to make precise P_{3D} predictions from nonlinear to arbitrarily large (linear) scales even when using simulations with moderate sizes as training data. It also enables predicting any Lyman- α statistic derived from P_{3D} without requiring interpolation or extrapolation. For instance, we can compute ξ_{3D} by taking the Fourier transform of P_{3D} or determine P_{1D} by integrating its perpendicular modes

$$P_{1D}(k_{\parallel}) = (2\pi)^{-1} \int_0^{\infty} dk_{\perp} k_{\perp} P_{3D}(k_{\parallel}, k_{\perp}), \quad (1)$$

where k_{\parallel} and k_{\perp} indicate parallel and perpendicular modes, respectively.

We emulate the 8 previous parameters as a function of cosmology and IGM physics using FORESTFLOW¹, a conditional normalizing flow (cNFs; Winkler et al. 2019; Papamakarios et al. 2019). FORESTFLOW predicts the values and correlations of model parameters, allowing to propagate these correlations onto P_{3D} and derived statistics. We train FORESTFLOW using measurements from the suite of cosmological hydrodynamical simulations presented in Pedersen et al. (2021), which consists of 30 fixed-and-paired hydrodynamical simulations of 67.5 Mpc on a side.

The release of FORESTFLOW is quite timely for BAO and P_{1D} analyses of the ongoing Dark Energy Spectroscopic Instrument survey (DESI; DESI Collaboration et al. 2016), which will quadruple the number of line-of-sights observed by first the Baryon Oscillation Spectroscopic Survey (BOSS; Dawson et al. 2013) and its extension (eBOSS; Dawson et al. 2016). DESI has already proven the constraining power of Lyman- α studies by measuring the isotropic BAO

scale with $\simeq 1\%$ precision from the Data Release 1 (DESI Collaboration et al. 2024a) and P_{1D} at 9 redshift bins with a precision of a few percent from the Early Data Release (Ravoux et al. 2023; Karaçaylı et al. 2024). In addition to being used for BAO and P_{1D} studies, FORESTFLOW has the potential to extend towards non-linear scales the current full-shape analyses of ξ_{3D} (Cuceu et al. 2023; Gerardi et al. 2023) and P_{3D} (Font-Ribera et al. 2018; de Belsunce et al. 2024; Horowitz et al. 2024), and can be used to interpret alternative three-dimensional statistics (Hui et al. 1999; Font-Ribera et al. 2018; Karim et al. 2023).

The outline of this paper is as follows. We describe the emulation strategy in §2 and the suite of cosmological hydrodynamical simulations we use for training, how we measure P_{3D} and P_{1D} from these simulations, and our approach for computing the best-fitting parameters of the P_{3D} analytic model to these statistics in §3. In §4 and §5, we present FORESTFLOW and evaluate its performance using multiple tests. In §6, we discuss some possible uses for this emulator, and we summarize our main results and conclude in §7.

Throughout this paper, all statistics and distances are in comoving units.

2 EMULATION STRATEGY

This paper aims to develop FORESTFLOW, a Lyman- α forest emulator predicting the 2 Lyman- α linear biases and 6 parameters capturing small-scale deviations of P_{3D} from linear theory. We describe the emulation strategy in §2.1 and detail the input and output parameters of the emulator in §2.2.

2.1 P_{3D} parametric model

We can express fluctuations in the Lyman- α forest flux as $\delta_F(\mathbf{s}) = \bar{F}^{-1}(\mathbf{s})F(\mathbf{s}) - 1$, where $F = \exp(-\tau)$ and \bar{F} are the transmitted flux fraction and its mean, respectively, τ is the optical depth to Lyman- α absorption, and \mathbf{s} is the redshift-space coordinate. On linear scales, these fluctuations depend upon the matter field as follows (e.g.; McDonald 2003)

$$\delta_F = b_{\delta} \delta + b_{\eta} \eta, \quad (2)$$

where δ refers to matter density fluctuations, $\eta = -(aH)^{-1}(\partial v_r / \partial r)$ stands for the dimensionless line-of-sight gradient of radial peculiar velocities, a is the cosmological expansion factor, H is the Hubble expansion factor, v_r is the radial velocity, and r stands for the radial comoving coordinate. The linear bias coefficients b_{δ} and b_{η} capture the response of δ_F to large-scale fluctuations in the δ and η fields, respectively.

Following McDonald (2003), we decompose the three-dimensional power spectrum of δ_F into three terms

$$P_{3D}(k, \mu) = (b_{\delta} + b_{\eta} f \mu^2)^2 D_{NL}(k, \mu) P_{lin}(k), \quad (3)$$

where $f = d \log G / d \log a$ is the logarithmic derivative of the growth factor G , $(b_{\delta} + b_{\eta} f \mu^2)^2$ accounts for linear biasing and large-scale redshift space distortions (Kaiser 1987; McDonald et al. 2000a), P_{lin} is the linear matter power spectrum², and D_{NL} is a physically-motivated parametric correction accounting for the nonlinear growth of the density field, nonlinear peculiar velocities, thermal broadening, and pressure.

¹ Publicly available at <https://github.com/igmhub/ForestFlow>.

² This is the linear power spectrum of cold dark matter and baryons even for cosmologies with massive neutrinos.

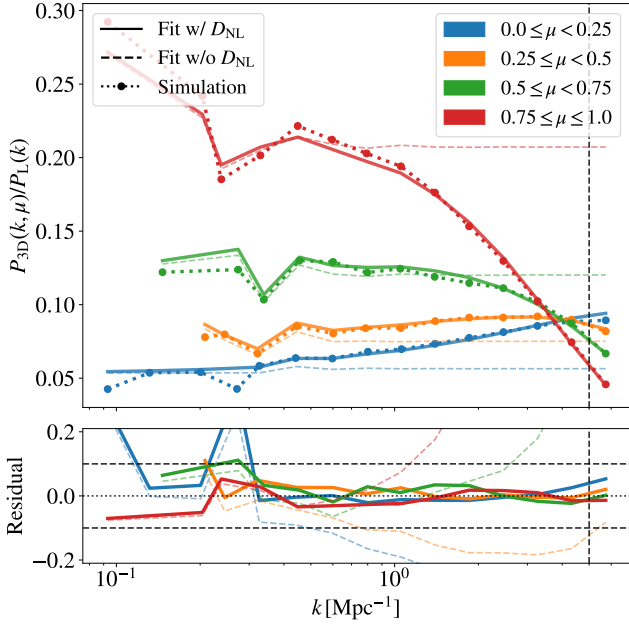


Figure 1. Precision of the P_{3D} model (see Eqs. 3 and 4) in reproducing measurements from the CENTRAL simulation at $z = 3$. The top panel shows the ratio of P_{3D} to the linear power spectrum: dotted lines represent simulation measurements, while solid and dashed lines indicate the ratio for the best-fitting model with and without small-scale corrections, respectively. Line colors correspond to different μ wedges, and vertical dashed lines mark the minimum scale used for computing the best-fitting model, $k = 5 \text{ Mpc}^{-1}$. The bottom panel displays the relative difference between the best-fitting model (with and without small-scale corrections) and simulation measurements. The overall precision of the model is 2% on scales in which simulation measurements are not strongly affected by cosmic variance ($k > 0.5 \text{ Mpc}^{-1}$; see text).

The large-scale behavior of P_{3D} is set by the bias coefficients b_δ and b_η together with the linear power spectrum, and the latter can be computed using a Boltzmann solver (e.g.; Lewis et al. 2000; Lesgourgues 2011). Therefore, the emulation of the 2 Lyman- α linear biases enables predicting P_{3D} on arbitrarily large (linear) scales³. In contrast with direct emulation of power spectrum modes, this approach only requires simulations large enough for measuring the 2 Lyman- α linear biases precisely.

Making predictions for P_{3D} on small scales is more challenging than on large scales due to the variety of effects affecting this statistics on the nonlinear regime (e.g.; McDonald 2003). In this work, we describe small-scale effects using the physically-motivated Arinyo-i-Prats et al. (2015) parameterization

$$D_{NL} = \exp \left\{ \left(q_1 \Delta^2 + q_2 \Delta^4 \right) \left[1 - \left(\frac{k}{k_v} \right)^{a_v} \mu^{b_v} \right] - \left(\frac{k}{k_p} \right)^2 \right\}, \quad (4)$$

where $\Delta^2(k) \equiv (2\pi^2)^{-1} k^3 P_{lin}(k)$ is the dimensionless linear matter power spectrum, μ is the cosine of the angle between the Fourier mode and the line of sight, and the free parameters k_v and k_p are in Mpc^{-1} units throughout this work. The terms involving $\{q_1, q_2\}$, $\{k_v, a_v, b_v\}$, and $\{k_p\}$ account for nonlinear growth, peculiar velocities and thermal broadening, and gas pressure, respectively. Our

emulator predicts the value of these 6 free parameters together with the 2 Lyman- α linear biases.

In the top panel of Fig. 1, we show the ratio of P_{3D} to the linear power spectrum: dotted and solid lines indicate simulation measurements and the best-fitting model to it (Eqs. 3 and 4), respectively. See §3 for details about this simulation and the fitting procedure. The dashed lines depict the results for the best-fitting model when setting $D_{NL} = 1$ after carrying out the fit; i.e., the behaviour of the best-fitting model on linear scales. We can readily see that nonlinear growth isotropically increases the power with growing k , while peculiar velocities and thermal broadening suppress the power of parallel modes. On the smallest scales shown, pressure takes over and causes an isotropic suppression of all modes. These effects modify the perpendicular power by 10% for scales as large as $k = 0.5 \text{ Mpc}^{-1}$, indicating that small-scale corrections affect most of the scales sampled by our simulations. Nevertheless, our simulations are large enough to measure the 2 Lyman- α linear biases with percent precision (see Appendix A).

On the largest scales, we find strong variations between consecutive k -bins for the same μ -wedge. Some of these oscillations are driven by differences in the average value of μ between consecutive bins due to the limited number of modes entering each bin on large scales. To ensure an accurate comparison between simulation measurements and model predictions, we individually evaluate the P_{3D} model for all the modes within each $k - \mu$ bin from our simulation boxes. We then calculate the mean of the resulting distribution and assign this mean value to the bin, thereby mirroring the approach used to compute P_{3D} measurements from the simulations. This process is crucial for large scales where the number of modes is small and nonlinear scales where the dependence of the number of modes with k is strong. We follow the same approach to evaluate the P_{3D} model throughout this work.

After accounting for the previous effect, the best-fitting model reproduces most large-scale oscillations. However, we can readily see a fluctuation at $k \simeq 0.25 \text{ Mpc}^{-1}$ in the $0 < \mu < 0.25$ wedge that it is not captured by the model. The difference between model predictions and simulation measurements for the bins adjacent to this one is approximately zero, suggesting that this fluctuation is caused by cosmic variance. We characterize the impact of this source of uncertainty in Appendix A, concluding that it can induce up to 10% errors on scales larger than $k = 0.5 \text{ Mpc}^{-1}$. Consequently, cosmic variance hinders our ability to evaluate the model's performance on the largest scales shown. However, this does not necessarily indicate a decrease in model precision on scales larger than $k = 0.5 \text{ Mpc}^{-1}$; rather, our simulations are simply not large enough to accurately assess the model's precision on such scales. In the bottom panel of Fig. 1, we can see that the average precision of the model is 2% for $k > 0.5 \text{ Mpc}^{-1}$, supporting the use of Eq. 4 for capturing small-scale deviations from linear theory.

2.2 Input and output parameters

In addition to the density and velocity fields, the Lyman- α forest depends upon the ionization and thermal state of the IGM (e.g.; McDonald 2003). Following Pedersen et al. (2021), we use 6 parameters to describe the dependency of this observable with cosmology and IGM physics:

- Amplitude (Δ_p^2) and slope (n_p) of the linear matter power spec-

³ Aside from nonlinear effects affecting the position and damping of BAO.

trum on small scales. These are defined as

$$\Delta_p^2(z) = k^3 P_{\text{lin}}(k_p, z), \quad (5)$$

$$n_p(z) = (d \log P_{\text{lin}} / d \log k) |_{k=k_p}, \quad (6)$$

where we use $k_p = 0.7 \text{ Mpc}^{-1}$ as the pivot scale because it is at the center of the range of interest for DESI small-scale studies. These parameters capture multiple physical effects modifying the linear power spectrum on small scales (see Pedersen et al. 2021, for a detailed discussion), including cosmological parameters such as the amplitude (A_s) and slope (n_s) of the primordial power spectrum, the Hubble parameter, and the matter density (Ω_m), or Λ CDM extensions such as curvature and massive neutrinos. The advantage of using this parameterization rather than Λ CDM parameters is twofold. First, we reduce the dimensionality of the emulator input, which decreases the number of simulations required for precise training. Second, the resulting emulator has the potential for making precise predictions for variations in cosmological parameters and Λ CDM extensions not considered in the training set (Pedersen et al. 2021; Pedersen et al. 2023; Cabayol-Garcia et al. 2023). Note that we do not consider cosmological parameters capturing changes in the growth rate or expansion history because the Lyman- α forest probes cosmic times during which the universe is practically Einstein de-Sitter, and both vary very little with cosmology in this regime.

- Mean transmitted flux fraction (\bar{F}). It depends on the intensity of the cosmic ionizing background and evolves strongly with redshift. One of the advantages of using this parameter is that it encodes the majority of the redshift dependence of the signal, serving as a proxy for cosmic time.

- Amplitude and slope of the temperature-density relation. The thermal state of the IGM can be approximated by a power law on the densities probed by the Lyman- α forest (Lukić et al. 2015): $T_0 \Delta_b^\gamma$, where Δ_b is the baryon overdensity, T_0 is the gas temperature at mean density, and γ is the slope of the relation. These parameters influence the ionization of the IGM, which is captured by \bar{F} , and the thermal motion of gas particles, which causes Doppler broadening that suppresses the parallel power. Instead of using T_0 as an emulator parameter, we follow Pedersen et al. (2021) and use the thermal broadening scale in comoving units. First, we express the thermal broadening in velocity units as $\sigma_T = 9.1(T_0[\text{K}]/10^4)^{1/2}$, and then we convert it to comoving units, $\sigma_T = \bar{\sigma}_T(1+z)H^{-1}$.

- Pressure smoothing scale. Gas pressure supports baryons on small scales, leading to a strong isotropic power suppression in this regime. The characteristic smoothing scale depends upon the entire thermal history of the gas (Gnedin & Hui 1998), and we parameterize its effect using the pressure smoothing scale in comoving units of Mpc^{-1} , k_F (see Pedersen et al. (2021) for more details).

Our emulator predicts the 8 free parameters of the P_{3D} model introduced by Eqs. 3 and 4, $\mathbf{y} = \{b_\delta, b_\eta, q_1, q_2, k_v, a_v, b_v, k_p\}$, as a function of the previous 6 parameters, $\mathbf{x} = \{\Delta_p^2, n_p, \bar{F}, \sigma_T, \gamma, k_F\}$. In the three next sections, we generate the training data of the emulator, discuss its implementation, and evaluate its precision.

3 TRAINING AND TESTING SET

In this section, we describe how we generate the training and testing data of our emulator. In §3.1, we present a suite of cosmological hydrodynamical simulations from which we generate mock Lyman- α forest measurements, and we detail our approach for extracting P_{3D} and P_{1D} measurements from these simulations in §3.2. In §3.3, we compute the best-fitting parameters of the model introduced by

Eqs. 3 and 4 to measurements of these statistics, and we evaluate the performance of the fits in §3.4.

3.1 Simulations

We extract Lyman- α forest measurements from a suite of simulations run with MP-GADGET⁴ (Feng et al. 2018; Bird et al. 2019), a massively scalable version of the cosmological structure formation code GADGET-3 (last described in Springel 2005). This suite of simulations was first presented and used in Pedersen et al. (2021); we briefly describe it next. Each simulation tracks the evolution of 768³ dark matter and baryon particles from $z = 99$ to $z = 2$ inside a box of $L = 67.5 \text{ Mpc}$ on a side, producing as output 11 snapshots uniformly spaced in redshift between $z = 4.5$ and 2. Two realizations were run for each combination of cosmological and astrophysical parameters using the “fixed-and-paired” technique (Angulo & Pontzen 2016; Pontzen et al. 2016), which significantly reduces cosmic variance for multiple observables, including the Lyman- α forest (Villaescusa-Navarro et al. 2018; Anderson et al. 2019).

To increase computational efficiency, the simulations utilize a simplified prescription for star formation that turns regions of baryon overdensity $\Delta_b > 1000$ and temperature $T < 10^5 \text{ K}$ into collisionless stars (e.g.; Viel et al. 2004), implement a spatially uniform ultra-violet background (Haardt & Madau 2012), and do not consider active galactic nuclei (AGN) feedback (e.g.; Chabanier et al. 2020). These approximations are justified because we focus on emulating the Lyman- α forest in the absence of astrophysical contaminants like AGN feedback, damped Lyman-alpha absorbers (DLAs), or metal absorbers, and we will model these before comparing our predictions with observational measurements (e.g.; McDonald et al. 2005; Palanque-Delabrouille et al. 2015, 2020).

We train FORESTFLOW using data from 30 fixed-and-paired simulations spanning combinations of cosmological and astrophysical parameters selected according to a Latin hypercube (McKay et al. 1979); we refer to these as TRAINING simulations hereafter. The Latin hypercube spans the parameters $\{\Delta_p^2(z = z_\star), n_p(z = z_\star), z_H, H_A, H_S\}$, where we use $z_\star = 3$ because it is approximately at the center of the range of interest for DESI studies (Ravoux et al. 2023; Karaçaylı et al. 2024), z_H is the midpoint of hydrogen reionization, and the last two parameters rescale the He II photoheating rate ϵ_0 as $\epsilon = H_A \Delta_b^{H_S} \epsilon_0$ (Oñorbe et al. 2017). Cosmological parameters were generated within the ranges $\Delta_p^2(z = z_\star) \in [0.25, 0.45]$, $n_p(z = z_\star) \in [-2.35, -2.25]$ by exploring values of the amplitude and slope of the primordial power spectrum within the intervals $A_s \in [1.35, 2.71] \times 10^{-9}$ and $n_s \in [0.92, 1.02]$. Any other Λ CDM parameter was held fixed to approximately Planck Collaboration et al. (2020) values: dimensionless Hubble parameter $h = 0.67$, physical cold dark matter density $\Omega_c h^2 = 0.12$, and physical baryon density $\Omega_b h^2 = 0.022$. As for the IGM parameters, these explored the ranges $z_H \in [5.5, 15]$, $H_A \in [0.5, 1.5]$, and $H_S \in [0.5, 1.5]$. All simulation pairs use the same set of initial Fourier phases, and thus cosmic variance affects in approximately the same way all combinations of input parameters.

We evaluate different aspects of the emulation strategy using 6 fixed-and-paired simulations with cosmological and astrophysical parameters not considered in the TRAINING simulations:

- The CENTRAL simulation uses cosmological and astrophysical parameters at the center of the TRAINING parameter space. We use this

⁴ <https://github.com/MP-Gadget/MP-Gadget/>

simulation for an out-of-sample test of the emulator's performance under optimal conditions, as the precision of machine-learning models typically decreases as we move closer to the border of the convex hull set by the training set.

- The SEED simulation uses the same parameters as the CENTRAL simulation while considering a different distribution of initial Fourier phases. Given that all TRAINING simulations use the same initial Fourier phases, SEED is useful to evaluate the impact of cosmic variance in the training set on FORESTFLOW predictions.

- The GROWTH, NEUTRINOS, and CURVED simulations adopt the same values of $\Delta_p^2(z_\star)$, $n_p(z_\star)$, physical cold dark matter and baryonic densities, and astrophysical parameters as the CENTRAL simulation. However, the GROWTH simulation uses 10% larger Hubble parameter ($h = 0.74$) and 18% smaller matter density ($\Omega_m = 0.259$) while using the same value of $\Omega_m h^2$ as the TRAINING simulations, the NEUTRINOS simulation includes massive neutrinos ($\sum m_\nu = 0.3$ eV), and the CURVED simulation considers an open universe ($\Omega_k = 0.03$). The NEUTRINOS and CURVED simulations also modify the value of the cosmological constant while holding fixed h to compensate for the increase in the matter density and the addition of curvature, respectively. The testing simulations address the precision of the emulation strategy for cosmologies not included in the training set.

- The REIONISATION simulation uses the same cosmological parameters as the CENTRAL simulation while implementing a distinct helium ionization history relative to the CENTRAL and TRAINING simulations (Puchwein et al. 2019). The main difference between the ionization histories of these simulations is that the one implemented in the REIONISATION simulation peaks at a later time than the others, leading to a significantly different thermal history. The REIONISATION simulation therefore tests the emulator's performance for thermal histories not considered in the TRAINING simulations.

3.2 Simulating Lyman- α forest data

To extract Lyman- α forest measurements from each simulation, we first select one of the simulation axes as the line of sight and displace the simulation particles from real to redshift space along this axis. Then, we compute the transmitted flux fraction along 768² uniformly-distributed line of sights along this axis using FSFE⁵ (Bird 2017); these lines of sight are commonly known as skewers. The resolution of the skewers is set to 0.05 Mpc, which is enough to resolve the thermal broadening and pressure scales, and are spaced by 0.09 Mpc in the transverse direction. We checked that P_{3D} and P_{1D} measurements within the range of interest (see §3.3) do not vary by increasing the line-of-sight resolution or the transverse sampling. After that, we repeat the previous steps for the three simulation axes to extract further cosmological information, as each simulation axis samples the velocity field in a different direction. Finally, we scale the effective optical depth of the skewers to 0.90, 0.95, 1.05, and 1.10 times its original value (see Lukić et al. 2015, for more details about this approach), which is equivalent to running simulations with different values of the UV background.

Using this data as input, we measure P_{3D} by first computing the three-dimensional Fourier transform of the skewers. Then, we take the average of the square norm of all modes within 20 logarithmically-spaced bins in wavenumber k from the fundamental mode of the box, $k_{\min} = 2\pi L^{-1} \simeq 0.09 \text{ Mpc}^{-1}$, to $k_{\max} = 40 \text{ Mpc}^{-1}$ and 16 linearly-spaced bins in the cosine of the angle between Fourier modes and the line of sight from $\mu = 0$ to 1. We measure P_{1D} by first computing the

one-dimensional Fourier transform of each skewer without applying any binning, and then by taking the average of the square norm of all these Fourier transforms.

We carry out these measurements for the 30 TRAINING and 6 test fixed-and-paired simulations, ending up with 2 (opposite Fourier phases) \times 3 (simulation axes) \times 11 (snapshots) \times 5 (mean flux rescalings) = 330 measurements per simulation. To reduce cosmic variance, we compute the average of measurements from different axes and phases of fixed-and-paired simulations, decreasing the number of measurements per simulation to 55. The training and testing sets of FORESTFLOW are thus comprised of 1650 and 330 Lyman- α power spectrum measurements, respectively. All these measurements are publicly available at <https://github.com/igmhub/LaCE>.

3.3 Fitting the parametric model

To generate training and testing data for our emulator, we compute the best-fitting parameters of Eqs. 3 and 4 to measurements from the simulations described in §3.1. We fit the model using P_{3D} measurements from $k = 0.09$ to 5 Mpc^{-1} and P_{1D} measurements from $k_{\parallel} = 0.09$ to 4 Mpc^{-1} . The size of our simulation boxes determines the largest scales used, while the maximum wavenumbers are set by the smallest scales measured by (Ravoux et al. 2023; Karaçaylı et al. 2024). We remind the reader that the large-scale behavior of P_{3D} is set by the 2 Lyman- α linear biases (see Eq. 3); consequently, the model can make accurate predictions for P_{3D} on arbitrarily large (linear) scales as long as these 2 parameters are measured precisely.

We compute the best-fitting value of model parameters $\mathbf{y} = \{b_\delta, b_\eta, q_1, q_2, k_v, a_v, b_v, k_p\}$ to simulation measurements by minimizing the pseudo- χ^2 :

$$\chi^2(\mathbf{y}) = \sum_i^{M_{3D}} w_{3D} \left[P_{3D}^{\text{data}}(k_i, \mu_i) - P_{3D}^{\text{model}}(k_i, \mu_i, \mathbf{y}) \right]^2 + \sum_i^{M_{1D}} w_{1D} \left[P_{1D}^{\text{data}}(k_{\parallel, i}) - P_{1D}^{\text{model}}(k_{\parallel, i}, \mathbf{y}) \right]^2, \quad (7)$$

where $M_{3D} = 164$ and $M_{1D} = 42$ are the number of P_{3D} and P_{1D} bins employed in the fit, respectively, the superscripts data and model refer to simulation measurements and model predictions, and w_{3D} and w_{1D} weigh the fit. We use the Nelder-Mead algorithm implemented in the routine MINIMIZE of SCIPY (Virtanen et al. 2020) to carry out the minimization⁶. The results of the fits are publicly accessible at <https://github.com/igmhub/ForestFlow>.

Ideally, we would use the covariance of P_{3D} and P_{1D} measurements as weight in the previous expression; however, we lack multiple realizations of the same simulation with different distributions of initial Fourier phases needed to estimate this covariance. In addition, its theoretical estimation is not straightforward (Maion et al. 2022). Instead, we disregard correlations between P_{3D} and P_{1D} and weigh these by $w_{3D} = N_{3D}(k, \mu)/(1 + \mu^2)^2$ and $w_{1D} = \alpha(1 + k_{\parallel}/k_0)^2$, where N_{3D} is the number of modes in each $k - \mu$ bin and $k_0 = 2 \text{ Mpc}^{-1}$. The terms involving N_{3D} , μ , and k_0 attempt to ensure an unbiased fit of P_{3D} and P_{1D} across the full range of scales used. The parameter $\alpha = 8000$ controls the relative weight of P_{3D} and P_{1D} in the fit, and its value is motivated by the different impact of cosmic variance on these (see Appendix A).

⁶ To ensure that this routine does not get stuck in a local minimum, we checked that the likelihood is unimodal in all cases using the Affine Invariant Markov chain Monte Carlo Ensemble sampler EMCEE (Foreman-Mackey et al. 2013).

⁵ https://github.com/sbird/fake_spectra.

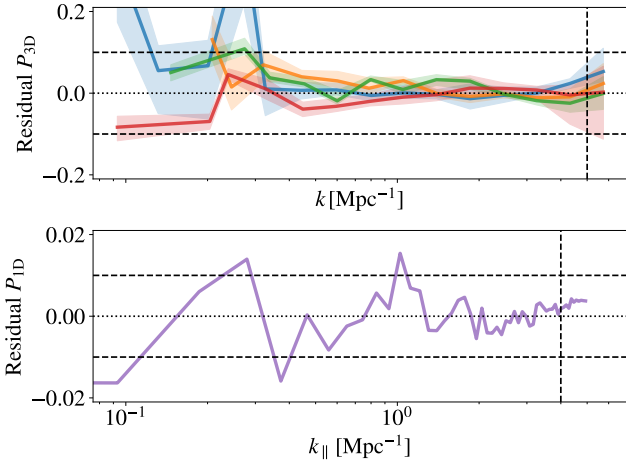


Figure 2. Precision of the parametric model (see Eqs. 3 and 4) in reproducing P_{3D} and P_{1D} measurements from all the TRAINING simulations. Lines and shaded areas show the mean and standard deviation of the relative difference between simulation measurements from the 1650 snapshots of the TRAINING simulations and best-fitting models to these, respectively. The precision of the model in recovering P_{3D} and P_{1D} is 2.4 and 0.6%, respectively, on scales not strongly affected by cosmic variance.

We expect significant correlations between the best-fitting value of the parameters to measurements from relatively small simulation boxes. As shown by Arinyo-i-Prats et al. (2015), these correlations are especially significant for the parameters accounting for nonlinear growth of structure, q_1 and q_2 . Givans et al. (2022) advocated for setting $q_2 = 0$ since this parameter is not necessary for describing P_{3D} at $z = 2.8$. However, we find non-zero values of this parameter indispensable for describing P_{3D} at redshifts below $z = 2.5$. This is not surprising since the gravitational evolution of density perturbations becomes increasingly more nonlinear as cosmic time progresses.

3.4 Precision of the model

In the previous section, we compute the best-fitting parameters of the P_{3D} model to measurements from the TRAINING simulations. Two main sources of uncertainty can affect these fits: cosmic variance and model inaccuracies. The first comes from the limited size of the TRAINING simulations, and it is amplified because they all use the same initial distribution of Fourier phases, meaning all simulations are subject to the same large-scale noise. We study this source of uncertainty in Appendix A, where we compare the best-fitting models to two simulations whose only difference is in their initial distribution of Fourier phases. Cosmic variance causes differences of 0.6 and 1.8% on the value of b_δ and b_η — equivalent to 1.2 and 1.8% for perpendicular and parallel P_{3D} modes on linear scales — and 0.8 and 0.1% on predictions for P_{3D} and P_{1D} from the best-fitting models, respectively, throughout the range of scales used in the fits. The second relates to using a parametric model with a limited number of free parameters to describe Lyman- α clustering.

In Fig. 2, we evaluate the performance of the parametric model in reproducing P_{3D} and P_{1D} measurements from the 1650 snapshots of the TRAINING simulations. As discussed in §2.1, cosmic variance hinders our ability to evaluate the precision of the model for P_{3D} on scales larger than $k = 0.5 \text{ Mpc}^{-1}$; motivated by this, we do so from this scale to the smallest one used in the fit, $k = 5 \text{ Mpc}^{-1}$. On

the other hand, since the impact of cosmic variance on P_{1D} is much smaller, we estimate the model performance for this statistic using all scales considered in the fit, $0.09 < k_\parallel [\text{Mpc}^{-1}] < 4$. We will follow the same approach when evaluating the precision of the emulator in §5. Under these considerations, the overall precision of the model in recovering P_{3D} and P_{1D} is 2.4 and 0.6%, respectively. Given that we estimate the precision of the model using our simulations, these numbers account for both the limited flexibility of the P_{3D} model and cosmic variance. The impact of the second on P_{3D} and P_{1D} measurements from our simulations is 1.3 and 0.5%, respectively, across the previous range of scales (see Appendix A). The precision for P_{1D} is practically the same in both cases and less than 1% worse for P_{3D} , letting us conclude that the P_{3D} model reproduces both statistics accurately.

4 FORESTFLOW

In this section we present FORESTFLOW, an emulator based on conditional normalizing flows that predicts the parameters of the P_{3D} model introduced by Eqs. 3 and 4 as a function of parameters capturing the dependence of the Lyman- α forest on cosmology and IGM physics. We detail its architecture and implementation in §4.1 and 4.2, respectively.

4.1 Conditional normalizing flows

Normalizing flows (NFs; Jimenez Rezendé & Mohamed 2015) are a class of machine-learning generative models designed to predict complex distributions by applying a sequence of bijective mappings to simple base distributions. A natural extension to this framework is conditional NFs (cNFs; Winkler et al. 2019; Papamakarios et al. 2019), a type of NFs that condition the mapping between the base and target distributions on a series of input variables. Given an input $\mathbf{x} \in X$ and target $\mathbf{y} \in Y$, cNFs predict the conditional distribution $p_{Y|X}(\mathbf{y}|\mathbf{x})$ by applying a parametric, bijective mapping $f_\phi : Y \times X \rightarrow Z$ to a base distribution $p_Z(\mathbf{z})$ as follows

$$p_{Y|X}(\mathbf{y}|\mathbf{x}) = p_Z(f_\phi(\mathbf{y}, \mathbf{x})|\mathbf{x}) \left| \frac{\partial f_\phi(\mathbf{y}, \mathbf{x})}{\partial \mathbf{y}} \right|, \quad (8)$$

where ϕ are the parameters of the mapping, while the last term of the previous equation is the Jacobian determinant of the mapping. In FORESTFLOW, the input is given by the parameters capturing the dependence of the Lyman- α forest on cosmology and IGM physics, $\mathbf{x} = \{\Delta_p^2, n_p, \bar{F}, \sigma_T, \gamma, k_F\}$, the target by the parameters of the P_{3D} model, $\mathbf{y} = \{b_\delta, b_\eta, q_1, q_2, k_v, a_v, b_v, k_p\}$, and the base distribution is an 8-dimensional Normal distribution $N^8(0, 1)$, where the dimension is determined by the number of P_{3D} model parameters.

Once trained, cNFs are a generative process from \mathbf{x} to \mathbf{y} . In our implementation, FORESTFLOW first samples randomly from the base distribution, and then it passes this realization through a sequence of mappings conditioned on a particular combination of cosmology and IGM parameters, $\tilde{\mathbf{y}} = f_\phi^{-1}(p_Z(\mathbf{z}), \mathbf{x})$, ending up with a prediction for the value of the P_{3D} parameters. Repeating this process multiple times, the FORESTFLOW yields a distribution of P_{3D} parameters $p_{\tilde{Y}|X}$ that, for a sufficiently large number of samples, approaches the target distribution $p_{Y|X}$. The breadth of this distribution captures uncertainties arising from the limited size of the training set. Finally, outside the cNF, we use each combination of P_{3D} parameters to evaluate Eqs. 3 and 1, obtaining predictions and uncertainties for P_{3D} and P_{1D} .

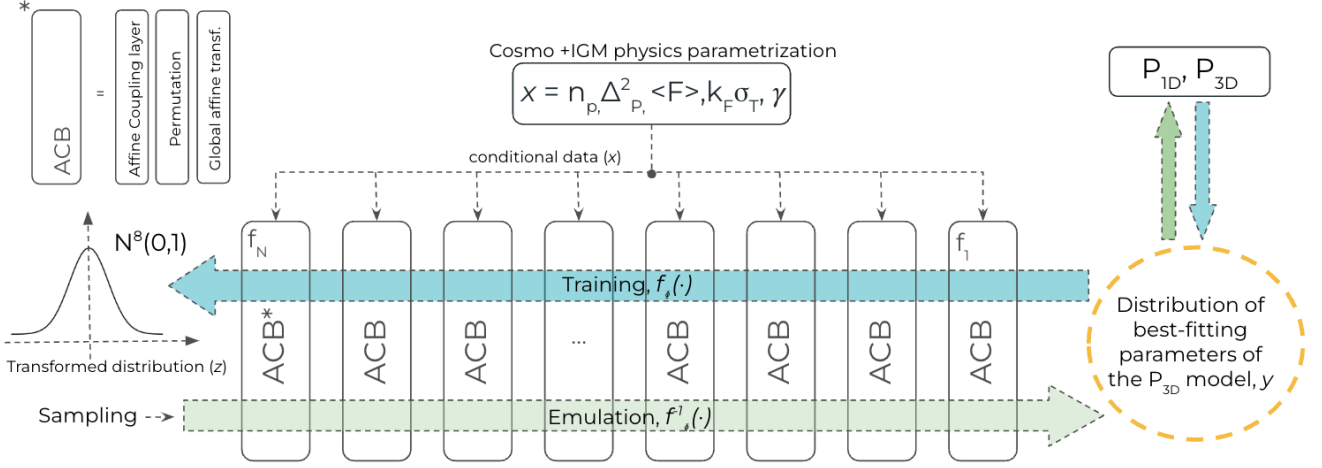


Figure 3. Architecture of FORESTFLOW, a Lyman- α forest emulator based on conditional Normalizing Flows. The blue arrow indicates the training direction, where FORESTFLOW optimizes a bijective mapping between the best-fitting parameters of the P_{3D} model to measurements from the TRAINING simulations and an 8-dimensional Normal distribution. The mapping is conditioned on cosmology and IGM physics and performed using 12 consecutive affine coupling blocks. The green arrow denotes the emulation direction, where the emulator applies the inverse of the mapping to random samples from the base distribution to predict the value of the P_{3D} model parameters. Outside the cNF, FORESTFLOW introduces these parameters in Eq. 3 and 1 to obtain predictions for P_{3D} and P_{1D} , respectively.

The main challenge when using cNFs is finding the mapping between the target and the base distribution, typically done using an N -layer neural network with bijective layers. This process runs in reverse relative to the generating process: we start by applying the mapping f_ϕ to the target data \mathbf{y} conditioned on the input \mathbf{x} , yielding \mathbf{z} . Then, we optimize the model parameters by minimizing the loss function

$$\mathcal{L} = \frac{1}{2} \sum \mathbf{z}^2 - \log \left| \frac{\delta f_\phi(\mathbf{y}, \mathbf{x})}{\delta \mathbf{y}} \right|. \quad (9)$$

We carry out this optimization process using stochastic gradient descent applied to minibatches, a methodology commonly employed for training neural networks.

4.2 Implementation

Neural Autoregressive Flows (Huang et al. 2018) use a series of invertible univariate operations to build a bijective transformation between a conditional distribution and a base distribution. In FORESTFLOW, we create a bijective mapping between the best-fitting parameters of the P_{3D} model and an 8-dimensional Normal distribution by applying $N_{ACB} = 12$ consecutive Affine-Coupling Block (ACB; Dinh et al. 2016) conditioned on cosmology and IGM physics. The transformation goes from the best-fitting parameters of the P_{3D} model to the base distribution when training the model, and in the opposite direction when evaluating it.

Each ACB conducts a series of operations $g_{i, \tilde{\phi}_i}$ on its input data \mathbf{w}_i , with i going from 1 to N_{ACB} and $\tilde{\phi}_i$ standing for the parameters of the transformation. First, it splits the input data into two subsamples with approximately the same number of elements, \mathbf{w}'_i and \mathbf{w}''_i . Then, it applies an affine transformation to the first subsample \mathbf{w}'_i

$$T(\mathbf{w}'_i) = \alpha_i \mathbf{w}'_i + \beta_i, \quad (10)$$

where α_i and β_i are neural networks with a single hidden layer of 128 neuron units. Third, the ACB merges the output from the affine transformation and the unchanged subsample, and then it applies a permutation layer to randomly rearrange these elements, obtaining $\tilde{\mathbf{w}}_i$. Fourth, the ACB applies an affine transformation to this sample,

$\tilde{T}(\tilde{\mathbf{w}}_i)$. The first and second affine transformations involve a subset of the training set and the entire training set, respectively, enabling the model to capture local and global features.

In Fig. 3, we show the architecture of FORESTFLOW. The blue arrow indicates the training direction, while the green arrow depicts the emulation direction. In the training direction, the input to the first ACB, $\mathbf{u}_1 = \mathbf{w}_1$, is a 1650-dimensional array composed of 14-dimensional vectors, where 1650 is the number of simulation snapshots in the training set. Each vector includes the 8 best-fitting P_{3D} model parameters to each snapshot and the 6 parameters describing the cosmology and IGM physics of this snapshot. The input to the i ACB, \mathbf{u}_i , is a 1650-array containing 14-dimensional vectors with the output of the $i - 1$ ACB and, once again, the 6 parameters describing the cosmology and IGM physics of each snapshot. Each ACB applies a transformation $f_{i, \phi_i} = g_{i, \tilde{\phi}_i}$, and the consecutive application of all ACBs results in the mapping between the target and the base distributions $\mathbf{z} = f_\phi(\mathbf{y}, \mathbf{x})$, where $f_\phi = \prod_{i=1}^{N_{ACB}} f_{i, \phi_i}$.

In the emulation direction, the input to the first ACB, $\mathbf{v}_1 = \mathbf{w}_1$, is a 14-dimensional vector containing random draws from an 8-dimensional Normal distribution and the 6 parameters describing the cosmology and IGM physics for which we want to obtain predictions. As in the training direction, the input to each subsequent ACB relies on the output from the previous ACB, each conditioned on cosmology and IGM physics. The ACBs apply the transformations $f_{i, \phi_i}^{-1} = g_{i, \tilde{\phi}_i}^{-1}$, which are the inverse of the corresponding transformations in the training direction, f_{i, ϕ_i} . FORESTFLOW makes predictions for P_{3D} model parameters by applying the composition of the inverse of all ACBs to random samples from the base distribution, $\tilde{\mathbf{y}} = f_\phi^{-1}(p_Z(\mathbf{z}), \mathbf{x})$, where $f_\phi^{-1} = \prod_{i=1}^{N_{ACB}} f_{i, \phi_i}^{-1}$.

We implement the emulator within the FreIA framework (Ardizzone et al. 2022), which uses PyTorch (Paszke et al. 2017) in the backend. FORESTFLOW is trained by minimizing Eq. 9 using an Adam optimizer (Kingma & Ba 2015) for 300 epochs with an initial learning rate of 10^{-3} . To select these and other hyperparameters, we use the Optuna framework (Akiba et al. 2019). First, Optuna trains FORESTFLOW for a particular combination of hyperparameters. Then, it computes the average value of Eq. 7 for all

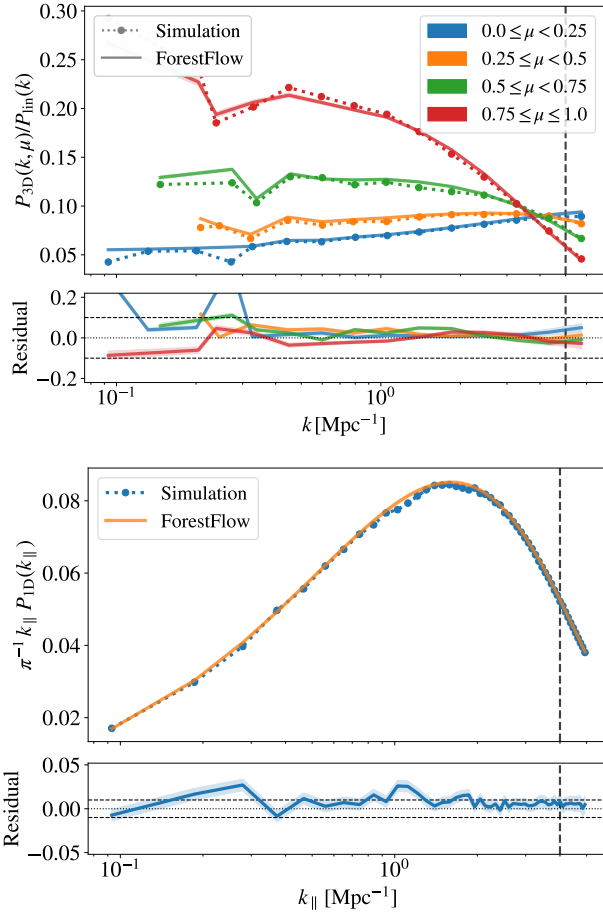


Figure 4. Precision of the emulator in recovering P_{3D} and P_{1D} measurements from the CENTRAL simulation at $z = 3$. Dotted lines show measurements from simulations, solid lines and shaded areas display the average and 68% credible interval of FORESTFLOW predictions, respectively, and vertical dashed lines indicate the minimum scales considered for computing the training data of the emulator. The overall precision of the emulator in recovering P_{3D} is 2.0% on scales not strongly affected by cosmic variance and 0.6% for P_{1D} .

simulations in the training set. After that, depending on the goodness of the fit to P_{3D} and P_{1D} measurements, Optuna selects a new value of the hyperparameters. We iterate with Optuna 50 times through a hyperparameter grid, selecting the hyperparameters that yield the highest precision. FORESTFLOW is publicly available at <https://github.com/igmhub/ForestFlow>.

5 EMULATOR PERFORMANCE

We evaluate the performance of FORESTFLOW in recovering P_{3D} and P_{1D} for cosmologies and IGM models included and not included in the training set in §5.1 and §5.2, respectively.

5.1 Cosmologies included in the training set

In this section, we evaluate the precision of FORESTFLOW in recovering the 2 Lyman- α linear biases, which determine the behavior of P_{3D} on linear scales, as well as P_{3D} and P_{1D} measurements from simulations on the intervals $0.5 < k [\text{Mpc}^{-1}] < 5$ and $0.09 < k_{\parallel} [\text{Mpc}^{-1}] < 4$, respectively. These are the ranges of scales used when fitting the

parametric model in §3 that are not strongly affected by cosmic variance (see §2.1). We begin by assessing the precision at the center of the training set, where machine-learning methods typically perform best, and then extend our evaluation across the entire input parameter space.

In Fig. 4, we compare measurements of P_{3D} and P_{1D} from the CENTRAL simulation at $z = 3$ with FORESTFLOW predictions. Dotted lines show simulation measurements, while solid lines and shaded areas display the average and 68% credible interval of FORESTFLOW predictions, respectively. We characterize the accuracy of the credible intervals in Appendix B. The overall precision of the emulator in recovering P_{3D} and P_{1D} is 2.0 and 0.6%, respectively. Note that cosmic variance hinders our ability to test the precision of the model; however, this does not necessarily indicate a decrease in model precision for P_{3D} on scales larger than $k = 0.5 \text{ Mpc}^{-1}$.

To better characterize the emulator's performance, we compute the average precision of FORESTFLOW in recovering measurements from CENTRAL across redshift. We find that it is 1.2 and 0.3% for b_{δ} and b_{η} , respectively, which translates into 1.1 and 1.2% for perpendicular and parallel P_{3D} modes on linear scales, and 2.6 and 0.8% for P_{3D} and P_{1D} . As discussed in §3.4, the precision of the parametric model in describing P_{3D} and P_{1D} measurements is 2.4 and 0.6%, respectively. Therefore, the primary factor limiting the performance of the emulator at the center of the parameter space is the quality of the training data, and its precision would increase by using bigger simulations with the same resolution to generate the training data.

We expect the emulator's efficiency to decrease away from the center of the input space. Ideally, we would have multiple test simulations covering the entire input space to evaluate the performance, but such simulations are unavailable. Instead, we conduct leave-one-out tests, which are widely used to assess the precision of an emulator when the number of training points is insufficient for out-of-sample tests (e.g.; Hastie et al. 2001). In a leave-one-out test, we optimize FORESTFLOW after removing a subsample from the training set; for example, all measurements from one of the TRAINING simulations. We then check the precision of the new emulator using the subsample held back. By repeating this process for other subsamples, we can estimate the performance of FORESTFLOW across the parameter space. Since each emulator is trained without using the entire dataset, leave-one-out tests provide a lower bound on emulator performance. Additionally, leave-one-out tests may require extrapolating the emulator's predictions, and it is widely known that machine-learning methods do not extrapolate well.

In the top panels of Fig. 5, lines and shaded areas display the average and standard deviation of 30 leave-simulation-out tests. Each test requires optimizing an emulator with 29 distinct TRAINING simulations, and then using the remaining simulation as the validation. Each panel shows the results for a different redshift, and we check that the results are similar for redshifts not shown. As we can see, the large-scale noise is similar for all TRAINING simulations; this is because they use the same initial distribution of Fourier phases. The performance of FORESTFLOW in recovering b_{δ} and b_{η} is 1.0 and 3.1%, respectively, which translates into 2.0 and 2.9% for perpendicular and parallel P_{3D} modes on linear scales, and 3.4 and 1.8% for P_{3D} and P_{1D} . Consequently, the efficiency across the parameter space is approximately 2 times worse than at the center for the 2 Lyman- α linear biases and P_{1D} , while it is 31% worse for P_{3D} . These numbers would likely improve by increasing the number of training simulations; nevertheless, the precision estimated via leave-one-out tests is always worse than at the center of the training set for

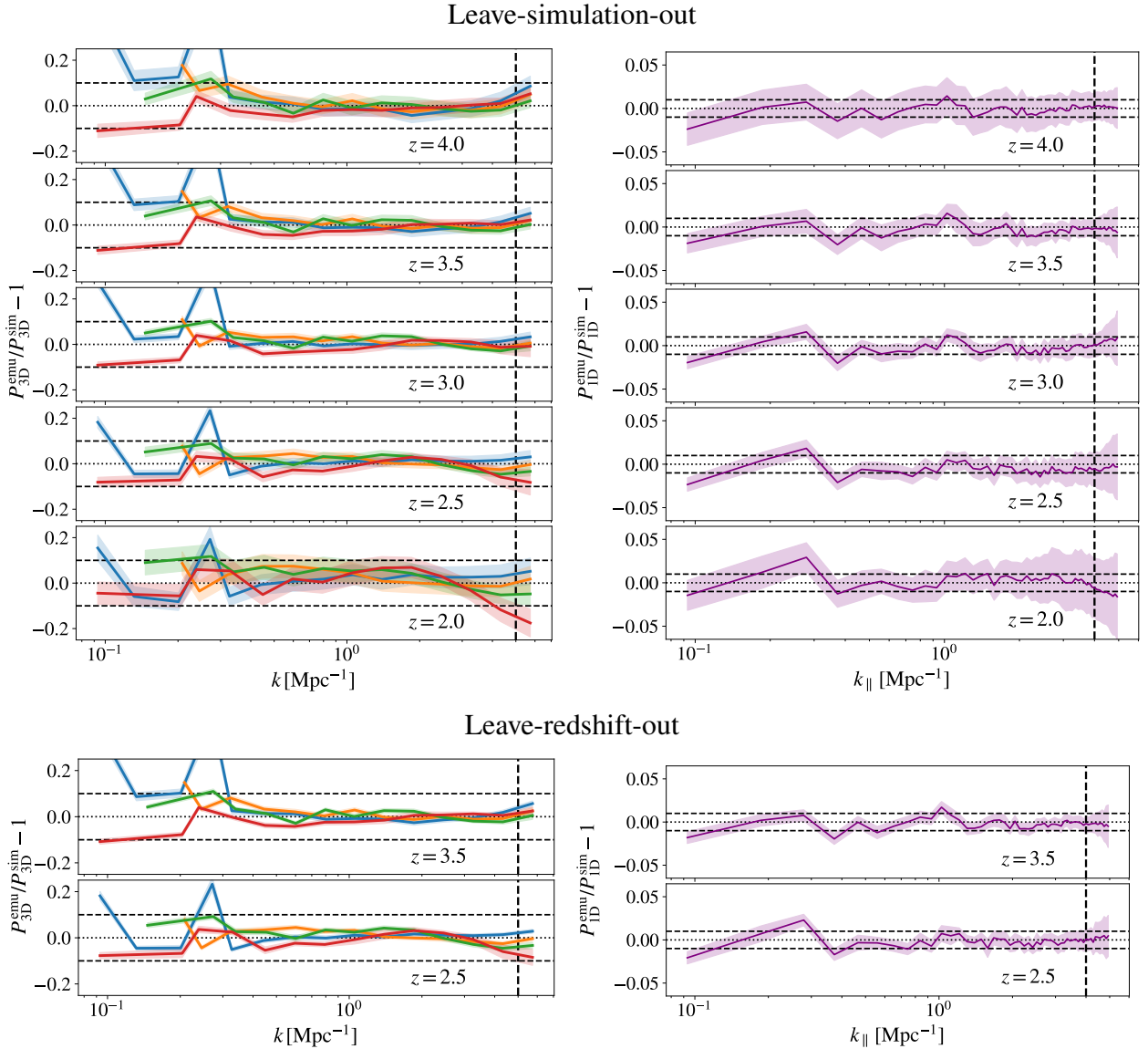


Figure 5. Precision of the emulator across the input parameter space estimated via leave-simulation-out (top panels) and leave-redshift-out tests (bottom panels). **Top panels.** Each leave-simulation-out test involves training 1 independent emulator with measurements from 29 distinct simulations, and then using the measurements from the remaining simulation as the validation set. Lines and shaded areas show the average and standard deviation of 30 leave-simulation-out tests, and each panel shows the results for a different redshift. **Bottom panels.** Leave-redshift-out tests require optimizing 1 emulator with all measurements but the ones at a particular redshift, and then using measurements from this redshift as validation. Each panel shows the results of a different test.

a small number of simulations because it often requires extrapolating the emulator's predictions.

By considering the results at the center and across the parameter space, we conclude that the size and number of the TRAINING simulations have a similar impact on the performance of FORESTFLOW. Given that leave-one-out tests only provide a lower bound for the emulator's performance, we conclude that the precision of FORESTFLOW in predicting P_{3D} from linear scales to $k = 5 \text{ Mpc}^{-1}$ is approximately 3%, and $\approx 1.5\%$ for P_{1D} down to $k_{\parallel} = 4 \text{ Mpc}^{-1}$.

As discussed in section 2.2, FORESTFLOW uses as input parameters measured from each snapshot of the training simulations rather than "traditional" cosmological parameters such as Ω_m , A_s , or H_0 . This strategy enables training FORESTFLOW without specifying the input redshift and making predictions for redshifts not present in the training set. To test this assumption, we carry out two leave-redshift-out

tests. The first involves optimizing one emulator with all TRAINING measurements but the ones at $z = 2.5$, and then validating it with data from this redshift. For the second, we follow the same approach but using measurements at $z = 3.5$. We display the results of these tests in the bottom panels of Fig. 5. The precision of the emulator is similar for leave-redshift-out and leave-simulation-out tests, validating the approach mentioned above. We find similar results for leave-redshift-out tests at other redshifts.

5.2 Test simulations

In Fig. 6, we examine the precision of FORESTFLOW reproducing P_{3D} and P_{1D} measurements from simulations outside the training set. Lines indicate the redshift average of the relative difference between model predictions and simulation measurements. The first two rows

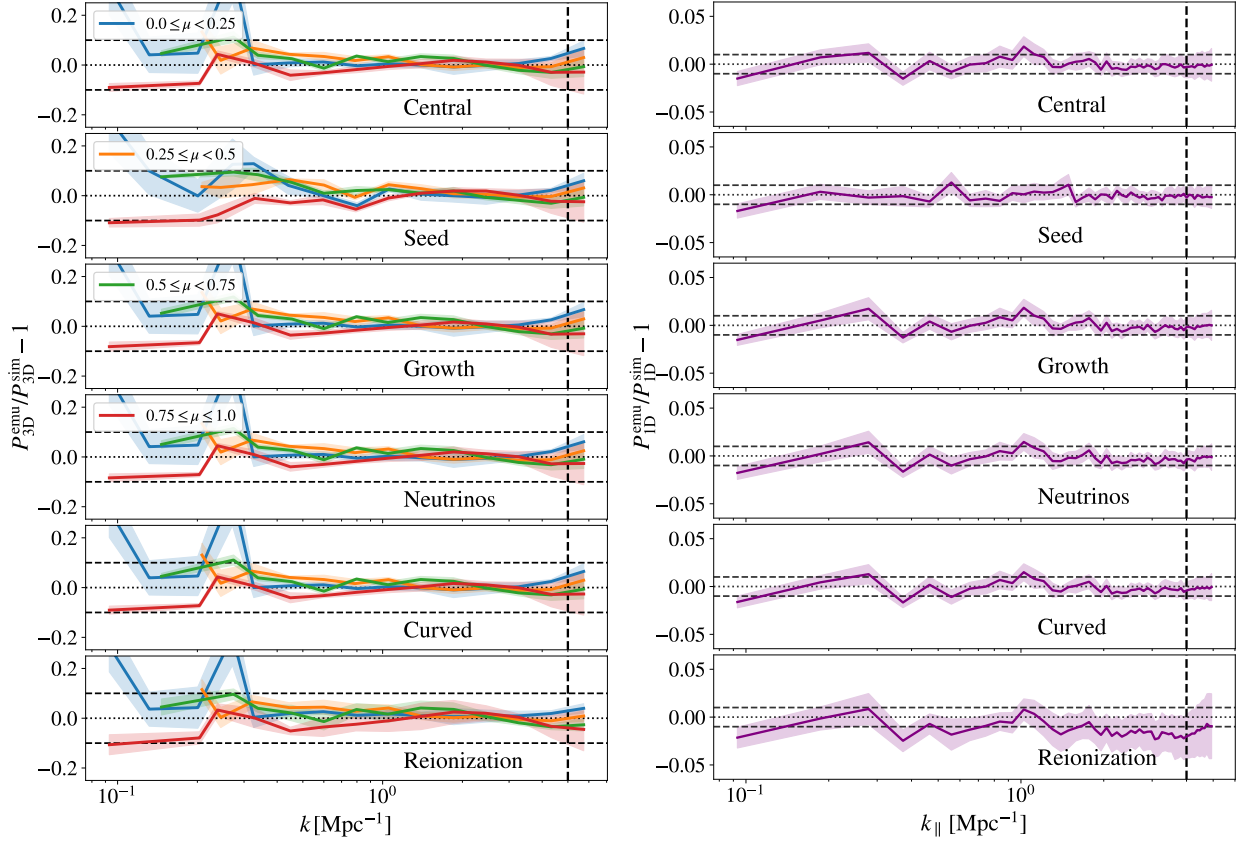


Figure 6. Precision of the emulator in recovering P_{3D} and P_{1D} for test simulations not included in the training set. Lines and shaded areas display the average and standard deviation of the results for 11 snapshots between $z = 2$ and 4.5 , respectively. From top to bottom, the rows show the results for the CENTRAL, SEED, GROWTH, NEUTRINOS, CURVED, and REIONISATION simulations, where the CENTRAL and SEED simulations are at the center of the input parameter space and employ the same and different initial distribution of Fourier phases as the training simulations, respectively, the GROWTH and REIONISATION simulations use a different growth and reionization history relative to those used by the TRAINING simulations, and the NEUTRINOS and CURVED simulations consider massive neutrinos and curvature. The efficiency of FORESTFLOW is approximately the same for all simulations.

show the results for the CENTRAL and SEED simulations, whose only difference is their initial distribution of phases. Consequently, the predictions of FORESTFLOW are the same for both. As we can see, these simulations present a different large-scale pattern of fluctuations, signaling that are caused by cosmic variance. Once we ignore these, we find that the precision of FORESTFLOW is practically the same for both simulations. We can thus conclude that FORESTFLOW predictions are largely insensitive to the impact of cosmic variance on the training set.

In the third, fourth, and fifth rows of Fig. 6, we use the GROWTH, NEUTRINOS, and CURVED simulations to evaluate the precision of FORESTFLOW for three different scenarios not contemplated in the training set: different growth history, massive neutrinos, and curvature. As we can see, the precision of FORESTFLOW for all these simulations is approximately the same as for the CENTRAL simulation. These results support that using the small-scale amplitude and slope of the linear power spectrum to capture cosmological information enables setting precise constraints on growth histories and Λ CDM extensions not included in the training set (see also Pedersen et al. 2021; Pedersen et al. 2023; Cabayol-Garcia et al. 2023).

In the last row of Fig. 6, we examine the precision of FORESTFLOW for the REIONISATION simulation, which employs a He II reionization history significantly different from those used by the TRAINING simulations. The precision of the emulator for this and the CENTRAL

simulation is similar, which is noteworthy given that the performance of P_{1D} emulators for the REIONISATION is significantly worse than for the CENTRAL simulation (Cabayol-Garcia et al. 2023). The outstanding performance of FORESTFLOW is likely because the relationship between IGM physics and the parameters of the P_{3D} model is more straightforward than with P_{1D} variations.

6 DISCUSSION

Cosmological analyses of the Lyman- α forest come in two flavors: one-dimensional studies focused on small, non-linear scales and three-dimensional analyses of large, linear scales. With FORESTFLOW, we can now consistently model Lyman- α correlations from nonlinear to linear scales, enabling a variety of promising analyses that we discuss next.

6.1 Connecting large-scale biases with small-scale physics

Small-scale Lyman- α analyses use emulators to predict P_{1D} as a function of cosmology and IGM physics (e.g.; Pedersen et al. 2021; Pedersen et al. 2023; Cabayol-Garcia et al. 2023), while large-scale analyses use linear or perturbation theory models to predict ξ_{3D} together with Lyman- α linear bias parameters that need to be marginalized over. FORESTFLOW provides a relationship between IGM physics

and linear biases, enabling the use of P_{1D} studies to inform three-dimensional analyses and vice versa.

We could use FORESTFLOW to fit P_{1D} measurements to set constraints on b_δ and b_η and then use these as priors in three-dimensional studies, breaking degeneracies between large-scale bias parameters and cosmology. As a result, we could measure the amplitude of linear density and velocity fluctuations, $\sigma_8(z)$ and $f\sigma_8(z)$ rather than $b_\delta\sigma_8$ and $b_\eta f\sigma_8$ like in traditional Lyman- α forest analyses. Similarly, we could use measurements of linear bias parameters from three-dimensional analyses (du Mas des Bourboux et al. 2020; DESI Collaboration et al. 2024b) to make predictions for IGM parameters, which could be used as priors in P_{1D} studies.

To illustrate this application, we compare FORESTFLOW predictions for b_δ and β with measurements from observations. The analysis of BAO in the Lyman- α forest from the first data release of DESI yields $b_\delta = -0.108 \pm 0.005$ and $\beta = 1.74 \pm 0.09$ at $z = 2.33$ (DESI Collaboration et al. 2024a). FORESTFLOW predicts $b_\delta = -0.118$ and $\beta = 1.57$ for a *Planck* cosmology at the same redshift when using the best-fitting constraints on IGM parameters from table 4 of Walther et al. (2019), which were derived from high-resolution P_{1D} measurements. Even though the constraints on IGM parameters were derived using a P_{1D} emulator trained on simulations with possibly slightly different definitions of the IGM parameters, FORESTFLOW predictions and DESI measurements agree at the 2 sigma level, encouraging this new type of study.

6.2 Alcock-Paczynski on mildly non-linear scales

Thanks to the increasing precision of galaxy surveys, there is a growing interest in extracting cosmological information from increasingly smaller scales in three-dimensional analyses. An avenue to do so is to analyze anisotropies in the correlation function Alcock & Paczynski (AP test; 1979), first proposed in the context of the Lyman- α forest by McDonald & Miralda-Escudé (1999); Hui et al. (1999). Recently, Cuceu et al. (2023) followed this approach to analyze Lyman- α forest measurements from the Sloan Digital Sky Survey (SDSS) data release 16 (DR16; Ahumada et al. 2020), yielding constraints on some cosmological parameters a factor of two tighter than those from BAO-only analyses.

This study modeled three-dimensional correlations using linear theory, which restricted the range of scales analyzed to those larger than $25h^{-1}$ Mpc. We could significantly extend the range of scales used in this type of analysis by modeling three-dimensional correlations using FORESTFLOW. As a result, the constraining power of AP analyses would be much larger. Furthermore, we could use FORESTFLOW to extract information from P_{1D} analyses to reduce degeneracies between cosmology and the parameters describing ξ_{3D} (see §6.1).

6.3 Extending 3D analyses to the smallest scales

The ultimate goal of FORESTFLOW is to perform a joint analysis of one- and three-dimensional measurements from small to large scales. An interesting approach to do so is to measure the Lyman- α forest cross-spectrum (P_\times ; e.g.; Hui et al. 1999; Font-Ribera et al. 2018), which captures the correlation between one-dimensional Fourier modes from two neighboring quasars separated by a transverse separation (r_\perp). We can model this statistic by taking the inverse Fourier trans-

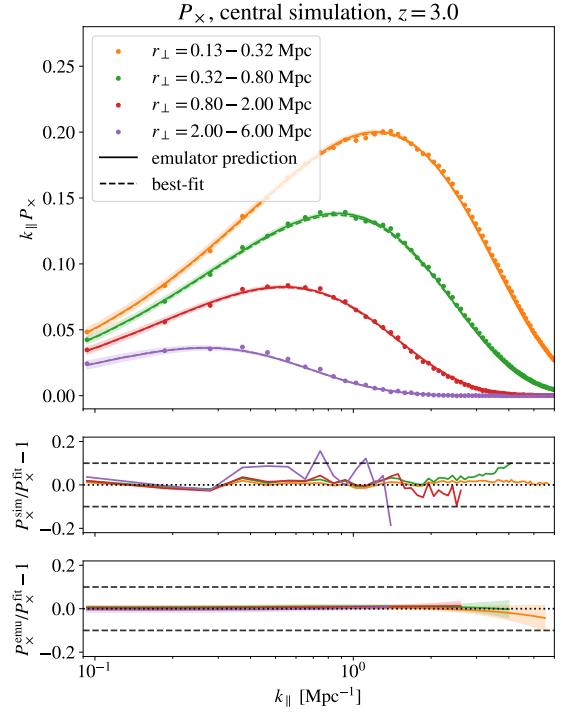


Figure 7. Precision of the parametric model and the emulator in describing P_\times measurements from the CENTRAL simulation at $z = 3$. Dots show simulation measurements, dashed lines depict predictions from the best-fitting parametric model to P_{3D} and P_{1D} measurements, and solid lines and shaded areas display the average and 68% credible interval of FORESTFLOW predictions. The color of the lines indicates the results for different bins in transverse separation r_\perp . The middle panel shows the residual between simulation measurements and the best-fitting model, while the bottom panel displays the residual between the best-fitting model and emulator predictions. The precision of FORESTFLOW in reproducing simulation measurements is approximately the same as the best-fitting model.

form of P_{3D} only along the perpendicular directions

$$P_\times(k_\parallel, r_\perp) \equiv \frac{1}{(2\pi)^2} \int d\mathbf{k}_\perp e^{i\mathbf{k}_\perp \cdot \mathbf{r}_\perp} P_{3D}(k_\parallel, k_\perp) \\ = \frac{1}{2\pi} \int_0^\infty dk_\perp k_\perp J_0(k_\perp r_\perp) P_{3D}(k_\parallel, k_\perp). \quad (11)$$

Comparing this equation with Eq. 1, it becomes clear that P_{1D} is a special case of P_\times , corresponding to the limit where the transverse separation is zero.

In §3.3, we optimize the P_{3D} model to describe measurements of P_{3D} and P_{1D} from the TRAINING simulations. Then, in §4, we use the distribution of best-fitting parameters as the training set for FORESTFLOW, which predicts the value of P_{3D} model parameters as a function of cosmology and IGM physics. Even though neither the best-fitting model nor FORESTFLOW use P_\times for their optimization, we can make predictions of P_\times for both. To do so, we first estimate P_{3D} using the value of the model parameters using Eq. 3, and then we integrate it using Eq. 11. We carry out the integration using the fast Hankel transform algorithm FFTlog (Hamilton 2000) implemented in the hank1 package (Karamanis & Beutler 2021).

We use P_\times measurements from the simulations described in §3.1 to evaluate the precision of FORESTFLOW for this statistic. We first define four bins in r_\perp , the transverse separation between skewers in configuration space, with edges 0.13, 0.32, 0.80, 2, and 6 Mpc. Then,

we measure P_{\times} using all pairs of skewers with r_{\perp} separation within the previous bins

$$P_{\times}(r_{\perp}, k_{\parallel}) = \left\langle \Re \left[\tilde{\delta}_i(k_{\parallel}) \tilde{\delta}_j^*(k_{\parallel}) \right] \right\rangle \quad (12)$$

where $\tilde{\delta}_i$ and $\tilde{\delta}_j^*$ stand for the Fourier transform of a skewer i and the complex conjugate of its partner j , respectively, the average $\langle \rangle$ includes all possible pairs in the bin without repetition or permutation, and \Re indicates that we only use the real part of the expression between brackets because the average of the imaginary part is zero. The r_{\perp} on the left-hand side denotes the effective center of the bin, accounting for the skewed distribution of r_{\perp} within each bin: the number of skewers separated by a small distance dr_{\perp} is proportional to r_{\perp} , and therefore the effective center is not at the halfway point. To compute P_{\times} at the effective center, we perform the integration using ten sub-bins within each r_{\perp} bin and calculate the average of these weighted by r_{\perp} .

In Fig. 7, we compare measurements of P_{\times} from the CENTRAL simulation at $z = 3$ with the best-fitting model to P_{3D} and P_{1D} measurements from this simulation and FORESTFLOW predictions. As we can see, P_{\times} decreases as the r_{\perp} separation increases; this is because more distant sightlines are sampling increasingly uncorrelated regions. In the middle panel, we examine the precision of the best-fitting model in describing the data, finding that it is better than 10% throughout all the scales shown. The bottom panel addresses the performance of FORESTFLOW relative to the best-fitting model so we can evaluate the precision of the emulator in the absence of cosmic variance. As we can see, the precision of the emulator in recovering the best-fitting model is better than 5% for all scales.

Future studies could use FORESTFLOW for extracting constraints on cosmology and IGM physics from the analysis of P_{\times} measurements (e.g.; Karim et al. 2023). Nevertheless, as with P_{1D} , these analyses would also require modeling multiple systematics affecting Lyman- α measurements such as damped Lyman- α systems, metal line contamination, and AGN feedback.

7 CONCLUSIONS

We present FORESTFLOW, a cosmological emulator that predicts Lyman- α clustering from linear to nonlinear scales. Using an architecture based on conditional normalizing flows, FORESTFLOW emulates the 2 linear Lyman- α biases and 6 physically-motivated parameters capturing small-scale deviations of the three-dimensional flux power spectrum (P_{3D}) from linear theory. We summarize the main results of this work below:

- The main advantage of our strategy, compared to emulating P_{3D} at a set of k -bins, is that FORESTFLOW can predict Lyman- α clustering on arbitrarily large (linear) scales when combined with a Boltzmann solver. Additionally, the emulator can make predictions for any statistics derived from P_{3D} without interpolation or extrapolation, including the two-point correlation function (ξ_{3D} , main statistic of large-scale studies), the one-dimensional Lyman- α flux power spectrum (P_{1D} , main statistic of small-scale studies), and the cross-spectrum (P_{\times} , promising statistic for full-scale studies).
- To train the emulator, we use the best-fitting value of the 8 model parameters to P_{3D} and P_{1D} measurements from a suite of 30 fixed- and-paired cosmological hydrodynamical simulations spanning 11 equally-spaced redshifts between $z = 2$ and 4.5. We emulate these parameters as a function of the small-scale amplitude and slope of the linear power spectrum, the mean transmitted flux fraction, the

amplitude and slope of the temperature-density relation, and the pressure smoothing scale (see Pedersen et al. 2021). We use this parameterization because it has the potential for making predictions for extensions to the Λ CDM model and ionization histories not included in the training set (Pedersen et al. 2023; Cabayol-Garcia et al. 2023).

- In §5.1, we show that the precision of FORESTFLOW in predicting P_{3D} from linear scales to $k = 5 \text{ Mpc}^{-1}$ is 3% and 1.5% for P_{1D} down to $k_{\parallel} = 4 \text{ Mpc}^{-1}$. Interestingly, the size and number of training simulations have a similar impact on the emulator’s performance, while uncertainties arising from the limited flexibility of the 8-parameter model are subdominant.

- In §5.2, we show that FORESTFLOW displays similar performance as before for two extensions to the Λ CDM model — massive neutrinos and curvature — and ionization histories not included in the training set.

The release of FORESTFLOW is timely for Lyman- α forest analyses with the ongoing Dark Energy Spectroscopic Instrument (DESI) survey. As noted in §6, FORESTFLOW enables a series of novel multiscale studies with DESI data, including connecting large- and small-scale analyses as well as extending three-dimensional analyses towards smaller scales.

ACKNOWLEDGEMENTS

JCM, LCG, ML, and AFR acknowledge support from the European Union’s Horizon Europe research and innovation programme (COSMO-LYA, grant agreement 101044612). AFR acknowledges financial support from the Spanish Ministry of Science and Innovation under the Ramon y Cajal program (RYC-2018-025210) and the PGC2021-123012NB-C41 project. IFAE is partially funded by the CERCA program of the Generalitat de Catalunya. The analysis has been performed at Port d’Informació Científica (PIC); we acknowledge the support provided by PIC in granting us access to their computing resources.

This material is based upon work supported by the U.S. Department of Energy (DOE), Office of Science, Office of High-Energy Physics, under Contract No. DE-AC02-05CH11231, and by the National Energy Research Scientific Computing Center, a DOE Office of Science User Facility under the same contract. Additional support for DESI was provided by the U.S. National Science Foundation (NSF), Division of Astronomical Sciences under Contract No. AST-0950945 to the NSF’s National Optical-Infrared Astronomy Research Laboratory; the Science and Technology Facilities Council of the United Kingdom; the Gordon and Betty Moore Foundation; the Heising-Simons Foundation; the French Alternative Energies and Atomic Energy Commission (CEA); the National Council of Humanities, Science and Technology of Mexico (CONAHCYT); the Ministry of Science and Innovation of Spain (MICINN), and by the DESI Member Institutions: <https://www.desi.lbl.gov/collaborating-institutions>. Any opinions, findings, and conclusions or recommendations expressed in this material are those of the author(s) and do not necessarily reflect the views of the U. S. National Science Foundation, the U. S. Department of Energy, or any of the listed funding agencies. The authors are honored to be permitted to conduct scientific research on Iolkam Du’ag (Kitt Peak), a mountain with particular significance to the Tohono O’odham Nation.

DATA AVAILABILITY

FORESTFLOW and all the notebooks used to generate the plots of this paper can be found in <https://github.com/igmhub/ForestFlow>, as well as all data points shown in the published graphs. The simulations utilized for training and testing the emulator are publicly accessible at <https://github.com/igmhub/LaCE>.

REFERENCES

- Ahumada R., et al., 2020, *ApJS*, **249**, 3
- Akiba T., Sano S., Yanase T., Ohta T., Koyama M., 2019, in Proceedings of the 25th ACM SIGKDD International Conference on Knowledge Discovery and Data Mining.
- Alcock C., Paczynski B., 1979, *Nature*, **281**, 358
- Anderson L., Pontzen A., Font-Ribera A., Villaescusa-Navarro F., Rogers K. K., Genel S., 2019, *The Astrophysical Journal*, **871**, 144
- Angulo R. E., Pontzen A., 2016, *Monthly Notices of the Royal Astronomical Society*, **462**, L1
- Angulo R. E., Baugh C. M., Frenk C. S., Lacey C. G., 2008, *MNRAS*, **383**, 755
- Ardizzone L., Bungert T., Draxler F., Köthe U., Kruse J., Schmier R., Sorrenson P., 2018–2022, Framework for Easily Invertible Architectures (FrEIA), <https://github.com/vislearn/FrEIA>
- Arinyo-i-Prats A., Miralda-Escudé J., Viel M., Cen R., 2015, *JCAP*, **2015**, 017
- Bird S., 2017, Astrophysics Source Code Library, [p. ascl:1710.012](https://ui.adsabs.harvard.edu/abs/2017ASCl..1710.012B)
- Bird S., Rogers K. K., Peiris H. V., Verde L., Font-Ribera A., Pontzen A., 2019, *J. Cosmology Astropart. Phys.*, **2019**, 050
- Bird S., et al., 2023, PRIYA: A New Suite of Lyman-alpha Forest Simulations for Cosmology (arxiv:2306.05471), [doi:10.48550/arXiv.2306.05471](https://arxiv.org/abs/2306.05471), <http://arxiv.org/abs/2306.05471>
- Bolton J. S., Viel M., Kim T. S., Haehnelt M. G., Carswell R. F., 2008, *Monthly Notices of the Royal Astronomical Society*, **386**, 1131
- Busca N. G., et al., 2013, *A&A*, **552**, A96
- Cabayol-Garcia L., Chaves-Montero J., Font-Ribera A., Pedersen C., 2023, *Monthly Notices of the Royal Astronomical Society*, **525**, 3499
- Cen R., Miralda-Escudé J., Ostriker J. P., Rauch M., 1994, *ApJ*, **437**, L9
- Chabanier S., Bornaud F., Dubois Y., Palanque-Delabrouille N., Yèche C., Armengaud E., Peirani S., Beckmann R., 2020, *Monthly Notices of the Royal Astronomical Society*, **495**, 1825
- Chabanier S., et al., 2023, *MNRAS*, **518**, 3754
- Chen S.-F., Vlah Z., White M., 2021, *J. Cosmology Astropart. Phys.*, **2021**, 053
- Croft R. A. C., Weinberg D. H., Katz N., Hernquist L., 1998, *ApJ*, **495**, 44
- Cuceu A., Font-Ribera A., Nadathur S., Joachimi B., Martini P., 2023, *Physical Review Letters*, **130**, 191003
- DESI Collaboration et al., 2016, *arXiv e-prints*, [p. arXiv:1611.00036](https://arxiv.org/abs/1611.00036)
- DESI Collaboration et al., 2024a, DESI 2024 IV: Baryon Acoustic Oscillations from the Lyman Alpha Forest, [doi:10.48550/arXiv.2404.03001](https://arxiv.org/abs/2404.03001)
- DESI Collaboration et al., 2024b, *arXiv e-prints*, [p. arXiv:2404.03001](https://arxiv.org/abs/2404.03001)
- Dawson K. S., et al., 2013, *AJ*, **145**, 10
- Dawson K. S., et al., 2016, *AJ*, **151**, 44
- Dinh L., Sohl-Dickstein J., Bengio S., 2016, *arXiv e-prints*, [p. arXiv:1605.08803](https://arxiv.org/abs/1605.08803)
- Feng Y., Bird S., Anderson L., Font-Ribera A., Pedersen C., 2018, *Zenodo*, <https://zenodo.org/record/2517111>
- Fernandez M. A., Ho M.-F., Bird S., 2022, *Mon. Not. Roy. Astron. Soc.*, **517**, 3200
- Font-Ribera A., McDonald P., Slosar A., 2018, *Journal of Cosmology and Astroparticle Physics*, **2018**, 003
- Foreman-Mackey D., Hogg D. W., Lang D., Goodman J., 2013, *PASP*, **125**, 306
- Gerardi F., Cuceu A., Font-Ribera A., Joachimi B., Lemos P., 2023, *MNRAS*, **518**, 2567
- Givans J. J., Hirata C. M., 2020, *Phys. Rev. D*, **102**, 023515
- Givans J. J., Font-Ribera A., Slosar A., Seeyave L., Pedersen C., Rogers K. K., Blas D., Iršič V., 2022, *arXiv:2205.00962* [astro-ph]
- Gnedin N. Y., Hui L., 1998, *Monthly Notices of the Royal Astronomical Society*, **296**, 44
- Haardt F., Madau P., 2012, *The Astrophysical Journal*, **746**, 125
- Hamilton A. J. S., 2000, *MNRAS*, **312**, 257
- Hastie T., Tibshirani R., Friedman J., 2001, *The Elements of Statistical Learning*. Springer Series in Statistics, Springer New York Inc., New York, NY, USA
- Horowitz B., de Belsunce R., Lukic Z., 2024, *arXiv e-prints*, [p. arXiv:2403.17294](https://arxiv.org/abs/2403.17294)
- Huang C.-W., Krueger D., Lacoste A., Courville A., 2018, *arXiv e-prints*, [p. arXiv:1804.00779](https://arxiv.org/abs/1804.00779)
- Hui L., Stebbins A., Burles S., 1999, *The Astrophysical Journal*, **511**, L5
- Iršič V., Viel M., Haehnelt M. G., Bolton J. S., Becker G. D., 2017, *Physical Review Letters*, **119**, 031302
- Ivanov M. M., 2024, *Phys. Rev. D*, **109**, 023507
- Jimenez Rezende D., Mohamed S., 2015, *arXiv e-prints*, [p. arXiv:1505.05770](https://arxiv.org/abs/1505.05770)
- Kaiser N., 1987, *Monthly Notices of the Royal Astronomical Society*, **227**, 1
- Karaçaylı N. G., et al., 2024, *Monthly Notices of the Royal Astronomical Society*, **528**, 3941
- Karamanis M., Beutler F., 2021, *arXiv preprint arXiv:2106.06331*
- Karim M. L. A., Armengaud E., Mention G., Chabanier S., Ravoux C., Lukić Z., 2023, *arXiv e-prints*, [p. arXiv:2310.09116](https://arxiv.org/abs/2310.09116)
- Kingma D. P., Ba J., 2015, in Bengio Y., LeCun Y., eds, 3rd International Conference on Learning Representations, ICLR 2015, San Diego, CA, USA, May 7–9, 2015, Conference Track Proceedings. <http://arxiv.org/abs/1412.6980>
- Lee K.-G., et al., 2015, *The Astrophysical Journal*, **799**, 196
- Lesgourgues J., 2011, The Cosmic Linear Anisotropy Solving System (CLASS) I: Overview, [doi:10.48550/arXiv.1104.2932](https://ui.adsabs.harvard.edu/abs/2011arXiv1104.2932L), <https://ui.adsabs.harvard.edu/abs/2011arXiv1104.2932L>
- Lewis A., Challinor A., Lasenby A., 2000, *ApJ*, **538**, 473
- Lukić Z., Stark C. W., Nugent P., White M., Meiksin A. A., Almgren A., 2015, *MNRAS*, **446**, 3697
- MacKay D. J., et al., 1998, NATO ASI series F computer and systems sciences, **168**, 133
- Maion F., Angulo R. E., Zennaro M., 2022, *J. Cosmology Astropart. Phys.*, **2022**, 036
- McCulloch W. S., Pitts W., 1943, *The bulletin of mathematical biophysics*, **5**, 115
- McDonald P., 2003, *The Astrophysical Journal*, **585**, 34
- McDonald P., Miralda-Escudé J., 1999, *ApJ*, **518**, 24
- McDonald P., Miralda-Escudé J., Rauch M., Sargent W. L. W., Barlow T. A., Cen R., Ostriker J. P., 2000a, *The Astrophysical Journal*, **543**, 1
- McDonald P., Miralda-Escudé J., Rauch M., Sargent W. L. W., Barlow T. A., Cen R., Ostriker J. P., 2000b, *ApJ*, **543**, 1
- McDonald P., et al., 2005, *The Astrophysical Journal*, **635**, 761
- McDonald P., et al., 2006, *The Astrophysical Journal Supplement Series*, **163**, 80
- McKay M. D., Beckman R. J., Conover W. J., 1979, *Technometrics*, **21**, 239
- McQuinn M., 2016, *Annual Review of Astronomy and Astrophysics*, **54**, 313
- Meiksin A. A., 2009, *Reviews of Modern Physics*, **81**, 1405
- Meiksin A., Bryan G., Machacek M., 2001, *MNRAS*, **327**, 296
- Miralda-Escudé J., Cen R., Ostriker J. P., Rauch M., 1996, *ApJ*, **471**, 582
- Molaro M., Iršič V., Bolton J. S., Lieu M., Keating L. C., Puchwein E., Haehnelt M. G., Viel M., 2023, *Mon. Not. Roy. Astron. Soc.*, **521**, 1489
- Oñorbe J., Hennawi J. F., Lukić Z., 2017, *The Astrophysical Journal*, **837**, 106
- Palanque-Delabrouille N., et al., 2015, *Journal of Cosmology and Astroparticle Physics*, **2015**, 045
- Palanque-Delabrouille N., Yèche C., Schöneberg N., Lesgourgues J., Walther M., Chabanier S., Armengaud E., 2020, *Journal of Cosmology and Astroparticle Physics*, **2020**, 038
- Papamakarios G., Nalisnick E., Jimenez Rezende D., Mohamed S., Lakshminarayanan B., 2019, *arXiv e-prints*, [p. arXiv:1912.02762](https://arxiv.org/abs/1912.02762)
- Paszke A., et al., 2017, in NIPS-W.
- Pedersen C., Font-Ribera A., Rogers K. K., McDonald P., Peiris H. V., Pontzen A., Slosar A., 2021, *J. Cosmology Astropart. Phys.*, **2021**, 033

1055 Pedersen C., Font-Ribera A., Gnedin N. Y., 2023, *The Astrophysical Journal*,
 1056 944, 223

1057 Planck Collaboration et al., 2020, *Astronomy & Astrophysics*, 641, A6

1058 Pontzen A., Slosar A., Roth N., Peiris H. V., 2016, *Physical Review D*, 93,
 1059 103519

1060 Puchwein E., Haardt F., Haehnelt M. G., Madau P., 2019, *Monthly Notices*
 1061 *of the Royal Astronomical Society*, 485, 47

1062 Ramachandra N., Chaves-Montero J., Alarcon A., Fadikar A., Habib S., Heit-
 1063 mann K., 2022, *Monthly Notices of the Royal Astronomical Society*, 515,
 1064 1927

1065 Ravoux C., et al., 2023, *Monthly Notices of the Royal Astronomical Society*,
 1066 526, 5118

1067 Rogers K. K., Peiris H. V., 2021a, *Phys. Rev. D*, 103, 043526

1068 Rogers K. K., Peiris H. V., 2021b, *Phys. Rev. Lett.*, 126, 071302

1069 Rogers K. K., Peiris H. V., Pontzen A., Bird S., Verde L., Font-Ribera A.,
 1070 2019, *J. Cosmology Astropart. Phys.*, 2019, 031

1071 Sacks J., Welch W. J., Mitchell T. J., Wynn H. P., 1989, *Statistical Science*,
 1072 4, 409

1073 Seljak U., et al., 2005, *Physical Review D*, 71, 103515

1074 Seljak U., Makarov A., McDonald P., Trac H., 2006a, *Phys. Rev. Lett.*, 97,
 1075 191303

1076 Seljak U., Slosar A., McDonald P., 2006b, *Journal of Cosmology and As-*
 1077 *troparticle Physics*, 2006, 014

1078 Slosar A., et al., 2011, *Journal of Cosmology and Astroparticle Physics*, 2011,
 1079 001

1080 Slosar A., et al., 2013, *Journal of Cosmology and Astroparticle Physics*, 2013,
 1081 026

1082 Spergel D. N., et al., 2003, *The Astrophysical Journal Supplement Series*,
 1083 148, 175

1084 Springel V., 2005, *MNRAS*, 364, 1105

1085 Takhtaganov T., Lukić Z., Müller J., Morozov D., 2021, *ApJ*, 906, 74

1086 Verde L., et al., 2003, *The Astrophysical Journal Supplement Series*, 148,
 1087 195

1088 Viel M., Haehnelt M. G., 2006, *Monthly Notices of the Royal Astronomical*
 1089 *Society*, 365, 231

1090 Viel M., Weller J., Haehnelt M. G., 2004, *Monthly Notices of the Royal*
 1091 *Astronomical Society*, 355, L23

1092 Viel M., Becker G. D., Bolton J. S., Haehnelt M. G., 2013, *Phys. Rev. D*, 88,
 1093 043502

1094 Villaescusa-Navarro F., et al., 2018, *ApJ*, 867, 137

1095 Virtanen P., et al., 2020, *NatMe*, 17, 261

1096 Walther M., Oñorbe J., Hennawi J. F., Lukić Z., 2019, *ApJ*, 872, 13

1097 Walther M., Armengaud E., Ravoux C., Palanque-Delabrouille N., Yèche C.,
 1098 Lukić Z., 2021, *J. Cosmology Astropart. Phys.*, 2021, 059

1099 Winkler C., Worrall D., Hoozeboom E., Welling M., 2019, *arXiv e-prints*, p.
 1100 [arXiv:1912.00042](https://arxiv.org/abs/1912.00042)

1101 Zaldarriaga M., Hui L., Tegmark M., 2001, *The Astrophysical Journal*, 557,
 1102 519

1103 de Belsunce R., Philcox O. H. E., Irsic V., McDonald P., Guy J., Palanque-
 1104 Delabrouille N., 2024, *arXiv e-prints*, p. [arXiv:2403.08241](https://arxiv.org/abs/2403.08241)

1105 du Mas des Bourboux H., et al., 2020, *The Astrophysical Journal*, 901, 153

APPENDIX A: COSMIC VARIANCE

Throughout this work, we train and test FORESTFLOW using simulations run employing the "fixed-and-paired" technique (Angulo & Pontzen 2016; Pontzen et al. 2016), which significantly reduces cosmic variance for the clustering of the Lyman- α forest (Anderson et al. 2019). Ideally, we would use multiple fixed-and-paired simulations with different initial distributions of Fourier phases to estimate the precision of measurements of these statistics from our simulations. However, we only have two simulations with these properties: CENTRAL and SEED. In this section, we use these two simulations to estimate the impact of cosmic variance on simulation measurements and best-fitting models.

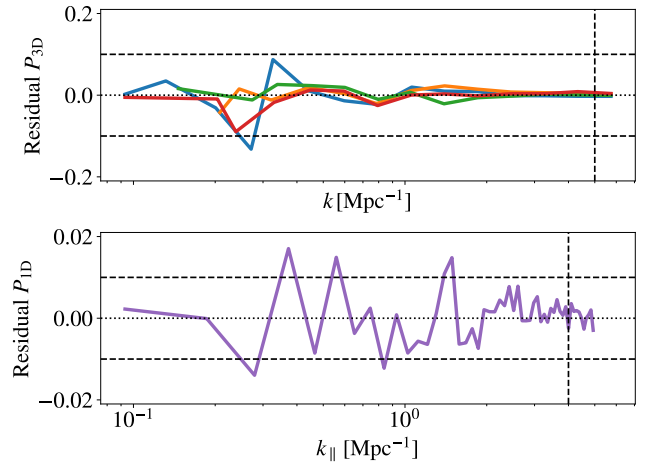


Figure A1. Impact of cosmic variance on measurements of P_{3D} (top panel) and P_{1D} (bottom panel) from our simulations at $z = 3$. Solid and dashed lines show the difference between measurements from CENTRAL and SEED divided by $\sqrt{2}$ times their average. We use the same color coding as in the main body. Cosmic variance induces errors as large as 10% on P_{3D} for $k \approx 0.3 \text{ Mpc}^{-1}$, while these are of the order of 1% for P_{1D} .

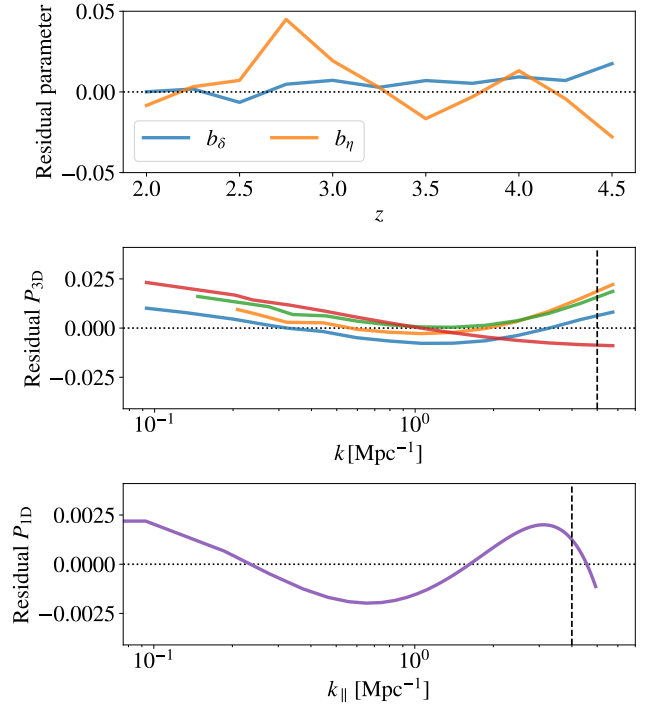


Figure A2. Impact of cosmic variance on predictions from the P_{3D} parametric model. Lines show the difference between the best-fitting model to the CENTRAL and SEED simulations, which only differ on their initial distribution of Fourier phases, divided by $\sqrt{2}$ times the best-fitting model to their average. The top panel shows the results for the Lyman- α linear biases, which sets P_{3D} on linear scales, while the middle and bottom panels display the results for P_{3D} and P_{1D} at $z = 3$ across the range of scales used in the fit. The impact of cosmic variance on b_δ and b_η is 0.6 and 1.8%, respectively, and 0.8 and 0.1% for P_{3D} and P_{1D} throughout the full range of scales shown.

In Fig. A1, we display the difference between measurements from the CENTRAL and SEED at $z = 3$ divided by $\sqrt{2}$ times their average. We employ the factor $\sqrt{2}$ to estimate the noise for a single simulation. In simulations with random initial conditions, the impact of cosmic variance on P_{3D} is inversely proportional to the square root of the number of modes, which grows with k^3 . However, in our fixed-and-paired simulations, errors reach approximately 10% at $k \approx 0.3 \text{ Mpc}^{-1}$ and decrease for larger and smaller scales. This is because the fix-and-paired technique completely cancels out cosmic variance for linear density modes but non-linear evolution (in particular mode coupling) re-introduces it on mildly non-linear scales (Maion et al. 2022). Consequently, this source of error hinders of ability to use our simulations to evaluate the precision of both the P_{3D} model and the emulator in §3.4 and 5, respectively. To mitigate the impact of cosmic variance in these tests, we restrict our analysis of P_{3D} to scales smaller than $k = 0.5 \text{ Mpc}^{-1}$, as these scales are less affected by cosmic variance. Conversely, P_{1D} measurements are minimally impacted by cosmic variance across all scales, allowing us to include the largest scales measured in the simulations without concern.

For a more precise estimation of the impact of cosmic variance on simulation measurements, we compute the standard deviation of the ratios shown in Fig. A1 using the 11 redshifts for which we have simulation measurements. We do so within the intervals $0.5 < k [\text{Mpc}^{-1}] < 5$ and $0.09 < k_{\parallel} [\text{Mpc}^{-1}] < 4$ for P_{3D} and P_{1D} , respectively, motivated by the previous discussion and the range of scales used when fitting the P_{3D} model in §3.3. We find that the average impact of cosmic variance on P_{3D} and P_{1D} is 1.3 and 0.5%, respectively. In what follows, we study the impact of this source of uncertainty on predictions from the best-fitting P_{3D} model to simulation measurements, which constitute the training data of FORESTFLOW.

In Fig. A2, we compare the best-fitting model to the CENTRAL and SEED simulations divided by the $\sqrt{2}$ times the best-fitting model to their average. We employ the factor $\sqrt{2}$ to estimate the noise for a single simulation. The CENTRAL and SEED simulations only differ on their initial distribution of Fourier phases, and thus differences in their fits provide an estimate for the impact of cosmic variance on the training data. In the top panel, we show the results for the 2 Lyman- α linear biases. As we can see, the differences between simulations reach almost 5% for b_{η} at $z = 2.75$, and the standard deviation of these for b_{δ} and b_{η} is 0.6 and 1.8%, respectively. Therefore, we can measure the 2 Lyman- α linear biases with percent level precision from our simulations. By propagating these uncertainties to the behavior of P_{3D} on linear scales, we find that the impact of cosmic variance on perpendicular and parallel modes is 1.2 and 1.8%, respectively.

In the middle and bottom panels of Fig. A2, we address the influence of cosmic variance on the best-fitting model predictions for P_{3D} and P_{1D} , respectively. The overall impact of this source of error on P_{3D} and P_{1D} is 0.8 and 0.1%, respectively, across the ranges of scales discussed above. These errors are significantly smaller than the impact of cosmic variance on simulation measurements, letting us conclude that the best-fitting model is less sensitive to cosmic variance than simulation measurements. Consequently, FORESTFLOW is more robust against this type of uncertainty than an emulator predicting the power spectrum at a set of k -bins.

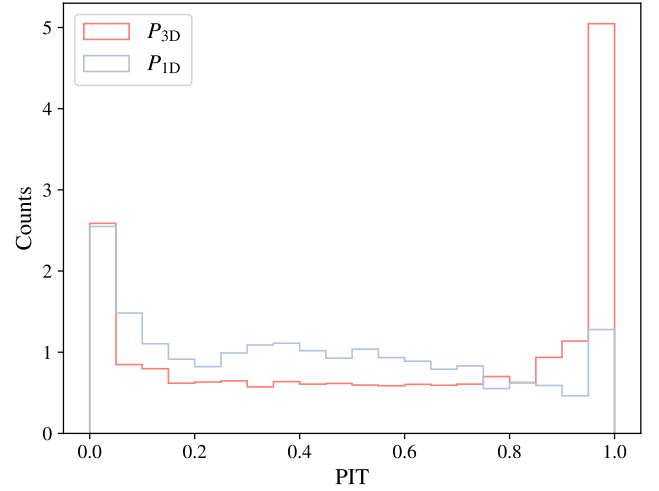


Figure B1. PIT distribution for P_{1D} (blue) and P_{3D} (red). This plot validates the uncertainties predicted by FORESTFLOW across TRAINING simulations via a leave-simulation-out approach. The PIT distribution is approximately uniform, indicating well-calibrated uncertainties for most samples, while the peaks at the edges indicate underestimated uncertainties for some samples.

APPENDIX B: P_{3D} AND P_{1D} UNCERTAINTY VALIDATION

Normalizing flows predict the full posterior distribution of the target data rather than only their mean like fully-connected neural networks or their mean and width like Mixture Density Networks (see Ramachandra et al. 2022; Cabayol-Garcia et al. 2023, for some applications in cosmology). This is achieved through multiple sampling iterations from the target latent distribution, an 8-dimensional Gaussian in our case. In FORESTFLOW, each sampled realization of the P_{3D} model parameters is propagated to generate predictions for P_{3D} and P_{1D} (see §4.1), producing a covariance matrix for these statistics. In this appendix, we validate its diagonal elements. Note that well-calibrated uncertainties are critical for future uses of the emulator such as cosmology inference.

We validate the uncertainty in P_{3D} and P_{1D} predictions using the Probability Integral Transform test (PIT), which is the value of the cumulative distribution function (CDF) of a distribution evaluated at the ground-truth value z_t

$$\text{PIT} = \text{CDF}[p, z_t] = \int_{-\infty}^{z_t} p(z) dz, \quad (\text{B1})$$

where p is in our case the distribution of FORESTFLOW predictions for P_{3D} or P_{1D} and z_t stands for measurements of these statistics from the simulations. A model that displays a well-calibrated uncertainty distribution yields PIT values that are uniformly distributed between zero and one. This indicates that the observed outcomes have an equal likelihood of falling at any point along the predicted CDF. In contrast, an excess of values close to zero or one indicates that the width of the distribution is underestimated.

In Fig. B1, we display a PIT test produced using all the TRAINING simulations via a leave-simulation-out approach (see §5.1). This process validates average predictions and uncertainties against simulations excluded in the training process. The red and blue lines display the results for P_{3D} and P_{1D} , respectively, which were generated by combining results from different scales and redshifts. As we can see, the PIT distribution is approximately uniform for both statistics but it presents peaks at the low and high ends, indicating underestimated

1208 uncertainties for some samples. The cause behind this feature is un-
1209 clear and it demands further investigation beyond the scope of this
1210 project.

1211 This paper has been typeset from a \LaTeX file prepared by the author.